Monthly Notices of the ROYAL ASTRONOMICAL SOCIETY

MNRAS **524,** 2814–2835 (2023) https://doi.org/10.1093/mnras/stad1966
Advance Access publication 2023 July 8

KURVS: the outer rotation curve shapes and dark matter fractions of $z \sim 1.5$ star-forming galaxies

Annagrazia Puglisi,[1,2★†] Ugnė Dudzevičiūtė,[3] Mark Swinbank,[2] Steven Gillman,[4,5] Alfred L. Tiley,[2,6] Richard G. Bower,[2,7,8] Michele Cirasuolo,[9] Luca Cortese,[6,10] Karl Glazebrook,[11] Chris Harrison,[12] Edo Ibar,[13] Juan Molina,[14] Danail Obreschkow,[6,15] Kyle A. Oman,[7,16] Matthieu Schaller,[17,18] Francesco Shankar[1] and Ray M. Sharples[19]

Affiliations are listed at the end of the paper

Accepted 2023 June 20. Received 2023 June 19; in original form 2023 January 16

ABSTRACT

We present first results from the KMOS Ultra-deep Rotation Velocity Survey (KURVS), aimed at studying the outer rotation curves shape and dark matter content of 22 star-forming galaxies at $z \sim 1.5$. These galaxies represent 'typical' star-forming discs at $z \sim 1.5$, being located within the star-forming main sequence and stellar mass-size relation with stellar masses $9.5 \leq \log(M_\star/\mathrm{M}_\odot) \leq 11.5$. We use the spatially resolved Hα emission to extract individual rotation curves out to 4 times the effective radius, on average, or ∼10–15 kpc. Most rotation curves are flat or rising between three and six disc scale radii. Only three objects with dispersion-dominated dynamics ($v_{\rm rot}/\sigma_0 \sim 0.2$) have declining outer rotation curves at more than 5σ significance. After accounting for seeing and pressure support, the nine rotation-dominated discs with $v_{\rm rot}/\sigma_0 \geq 1.5$ have average dark matter fractions of 50 ± 20 per cent at the effective radius, similar to local discs. Together with previous observations of star-forming galaxies at cosmic noon, our measurements suggest a trend of declining dark matter fraction with increasing stellar mass and stellar mass surface density at the effective radius. Measurements of simulated EAGLE galaxies are in quantitative agreement with observations up to $\log(M_\star R_{\rm eff}^{-2}/\mathrm{M}_\odot \mathrm{kpc}^{-2}) \sim 9.2$, and overpredict the dark matter fraction of galaxies with higher mass surface densities by a factor of ∼3. We conclude that the dynamics of typical rotationally-supported discs at $z \sim 1.5$ is dominated by dark matter from effective radius scales, in broad agreement with cosmological models. The tension with observations at high stellar mass surface density suggests that the prescriptions for baryonic processes occurring in the most massive galaxies (such as bulge growth and quenching) need to be reassessed.

Key words: galaxies: evolution – galaxies: high-redshift – galaxies: kinematics and dynamics.

1 INTRODUCTION

Some of the first evidence for dark matter in galaxy evolution dates back to 1978, when observations demonstrated that stars in the outer regions of luminous spiral galaxies (at radii up to ∼50 kpc, far beyond the stellar disc) rotate faster than expected from the gravity due to the observed gas and stars. This implied that most of the mass in these outer regions must be invisible (Bosma 1978; Rubin, Ford & Thonnard 1978). Since this first discovery, several other key measurements have converged to favour the existence of substantial amounts of dark matter within and outside of galaxies (e.g. Ostriker & Peebles 1973; Ostriker, Peebles & Yahil 1974; Frenk et al. 1985). Cold dark matter (CDM) now provides the framework for structures formation and is essential for the formation and evolution of galaxies in the ΛCDM paradigm. Most theoretical models in the last decades have thus included dark matter as a backbone for evolving galaxies in a cosmological context (Vogelsberger et al. 2014a; Schaye et al. 2015; Davé, Thompson & Hopkins 2016; Dubois et al. 2016, 2021; Davé et al. 2019; Springel et al. 2018; Pillepich et al. 2019, see also Vogelsberger et al. 2020 for a recent review). Cosmological simulations, built on ΛCDM theory, have had tremendous successes in recreating a universe with many characteristics similar to those of our own (Genel et al. 2014; Vogelsberger et al. 2014b; Furlong et al. 2017; Ferrero et al. 2017), and make specific predictions for the redshift evolution of baryonic and dark matter fractions within galaxies (e.g. Lovell et al. 2018).

Quantifying the mass and properties of baryons and dark matter haloes at early times is essential to better understand how galaxies assemble across cosmic history, and the main physical processes that shape their evolution. Eventually, studying dark matter at $1 \lesssim z \lesssim 3$, i..e cosmic noon, when galaxies are most efficiently forming stars and growing black holes at their centres (Madau & Dickinson 2014), can provide important constraints on the processes regulating its interaction with the baryonic matter. Measuring baryonic and dark matter masses in the distant Universe is challenging as galaxies become gradually smaller, less luminous and more irregular at

★ E-mail: a.puglisi@soton.ac.uk
† Anniversary Fellow.

© The Author(s) 2023.
Published by Oxford University Press on behalf of Royal Astronomical Society. This is an Open Access article distributed under the terms of the Creative Commons Attribution License (https://creativecommons.org/licenses/by/4.0/), which permits unrestricted reuse, distribution, and reproduction in any medium, provided the original work is properly cited.

Downloaded from https://academic.oup.com/mnras/article/524/2/2814/7221661 by University of Durham user on 31 October 2023

earlier cosmic times (e.g. Conselice 2014). However, advances in integral-field spectroscopic techniques have allowed us to measure the kinematics of galaxies beyond $z \gtrsim 1$, thus opening up the field of observational studies of the total mass budget at early times.

Dynamical studies with integral-field unit (IFU) spectrographs and observations at moderate to high spatial resolution in the sub-millimetre in the last decade have allowed us to characterize the kinematic properties of galaxies at cosmic noon and beyond (e.g. Lelli et al. 2018; Übler et al. 2018; Gillman et al. 2019; Molina et al. 2019; Sweet et al. 2019; Kaasinen et al. 2020; Fraternali et al. 2021; Herrera-Camus et al. 2022), also with the aid of gravitational lensing (e.g. Rizzo et al. 2020, 2021). Kinematic surveys reveal that galaxies on the star-forming main sequence are predominantly rotating discs (Förster Schreiber et al. 2009, 2018; Wisnioski et al. 2015, 2019; Stott et al. 2016). These galaxies appear to be different than massive discs at $z \sim 0$, as turbulent motions (probed by the velocity dispersion in spatially resolved spectra) provide a significant contribution to their dynamics (e.g. Weiner et al. 2006; Johnson et al. 2018; Übler et al. 2019). The fraction of rotating discs increases significantly since $z \sim 3.5$ (Turner et al. 2017b) and with increasing stellar mass at fixed redshift, suggesting that discs settle towards later times and that massive galaxies are more dynamically mature at a given cosmic epoch (a phenomenon that has been referred to as 'kinematic downsizing'; e.g. Kassin et al. 2012; Simons et al. 2017). To investigate the budget of visible and dark matter in disc galaxies and its evolution with redshift, dynamical surveys have exploited scaling relations such as the Tully–Fisher relation (Tully & Fisher 1977; Bell & de Jong 2001). This dynamical scaling relation compares the stellar mass (or the total baryonic mass, if considering the Baryonic Tully–Fisher relation; e.g. McGaugh et al. 2000; Lelli, McGaugh & Schombert 2016) to the rotation velocity, a tracer of the total dynamical mass, and hence provides information about the baryon and dark matter content of galaxies. A general consensus on the evolution of the Tully–Fisher relation as a function of redshift is still lacking, with some studies indicating mild or no evolution (Kassin et al. 2007; Miller et al. 2012; Harrison et al. 2017; Tiley et al. 2019a; Gogate et al. 2022) and others strong evolution (Cresci et al. 2009; Turner et al. 2017a; Übler et al. 2017).

Rotation curves describe the rotation velocity of the galaxy material as a function of galactocentric distance, and represent a more direct tool to probe the baryonic and dark matter content and radial distribution in and around galaxies. In the galaxy's central regions, stars and gas are expected to provide the dominant contribution to the rotation curve. Far from the galactic centre, rotation curves are expected to be flat if dark matter becomes the dominant mass component of the galaxies' outer discs. Observations extending out to the edge of the stellar and gaseous disc (∼10–15 kpc) are thus required to constrain the dark matter halo mass. IFU facilities at 8-meter class telescopes such as the Very Large Telescope have made possible to study rotation curves at high redshift. Recent studies using spatially resolved observations of the Hα emission line have suggested that some massive star-forming galaxies at $z \geq 1$ have declining rotation curves at large radii, potentially at odds with expectations from ΛCDM models (Genzel et al. 2017, 2020; Price et al. 2021, but see Lelli et al. 2023). It is still unclear how these results apply to the general star-forming population, and if dark matter fractions are a function of redshift, as also suggested by some Tully–Fisher evolution studies and statistical analyses of the total mass budget of galaxies (e.g. Wuyts et al. 2016), or other galaxy properties, such as the stellar mass. For example, deep observations indicate that $z \sim 1$ star-forming galaxies at $\log(M_\star/\mathrm{M}_\odot) \lesssim 10$, i.e. below the typical mass range probed by high-redshift surveys, show diverse shapes, ranging from rising to declining at large radii, and high dark matter fractions at scales of the stellar effective radius (Bouché et al. 2022). To understand if declining rotation curves and subsequently low dark matter fractions are the result of selection biases, and how rotation curve shapes and dark matter fractions are related to galaxy integrated properties and redshift, it is therefore essential to measure rotation curves in statistical samples covering a broad range in distant galaxy properties. However, dynamical surveys of $z \sim 1$–3 galaxies have typical integration times of 6-10 h (Förster Schreiber & Wuyts 2020) resulting in rotation curves of statistical samples that can be traced out to a few times the galaxy disc-scale radius, at best ($\sim R_{3D}$, equivalent to ∼1.8 times the half-light radius or ∼7 kpc), and this is not sufficient for probing rotation curves at large radii where dark matter starts to provide dominant contribution to potential. Some studies rely on stacking to access statistical samples and trace average rotation curves out to ∼15 kpc (e.g. Lang et al. 2017; Sharma et al. 2021), but it has been shown that stacking techniques are prone to systematics, and different assumptions can lead to differences in the implied dark matter fractions (Tiley et al. 2019b). Therefore, deep observations of statistical samples of *individual* galaxies spanning a broad range of distant galaxies' properties are needed, probing the outer radii where dark matter is expected to provide the dominant contribution to the disc dynamics.

In this context, the KMOS Ultra-deep Rotational Velocity Survey (KURVS) is designed to push the limit of the *K*-band Multi Object Spectrograph (KMOS) to measure the shape of the rotation curves in a statistical sample of main-sequence galaxies at $z \sim 1.5$ on a galaxy-by-galaxy basis out to (and beyond) six times the disc scale radius (∼10–16 kpc). This is achieved by exploiting the multiplex capabilities of KMOS (Sharples et al. 2013), which allows us to target up to 24 galaxies simultaneously, to observe the spatially resolved Hα emission for up to ∼80–100 h of integration per galaxy. In this paper, we describe the sample selection, observations and data reduction of KURVS. We then present measurements of the dynamical properties and outer rotation curve shapes of 22 KURVS galaxies in the Chandra Deep Field South (CDFS), each observed for ≈70 h on source. The spatially resolved gas-phase metallicity properties of this sample have been presented in Gillman et al. (2022). We use the GALPAK^{3D} parametric tool (Bouché et al. 2015) to correct the inner rotation curves for beam smearing, and measure dark matter fractions at the effective radius (∼2–4 kpc). We then compare our measurements of the outer rotation curve shapes and dark matter content with typical discs in the local Universe, as well as with measurements of the dark matter fraction in other samples of star-forming galaxies at cosmic noon. To interpret our results in the ΛCDM context, we compare our results to model star-forming galaxies from the EAGLE cosmological simulation (Crain et al. 2015; McAlpine et al. 2016).

This paper is structured as follows. In Section 2, we describe the sample selection and properties of the sample in the context of the parent star-forming population at similar cosmic epochs. We further describe the observing strategy and data reduction process. In Section 3, we describe the derivation of resolved properties and kinematics of the subset of KURVS galaxies in CDFS, putting our measurements in the context of wider IFU surveys. In this section, we also discuss measurements of the outer rotation curve shapes, the beam-smearing correction procedure, and measurements of the dark matter fraction at the effective radius. Additionally, we compare our measurements with previous results from the literature, as well as with simulations and local discs. Finally, we discuss our results in Section 4.

Downloaded from https://academic.oup.com/mnras/article/524/2/2814/7221661 by University of Durham user on 31 October 2023

Throughout this paper, we assume a Chabrier (2003) initial mass function and a standard ΛCDM cosmology ($H_0 = 70\,\mathrm{km\,s^{-1}\,Mpc^{-1}}$, $\Omega_\mathrm{m} = 0.3$, $\Omega_\Lambda = 0.7$).

2 THE KURVS SURVEY

KURVS is an ESO Large Programme (ID 1102.B-0232) designed to study the spatially resolved dynamics of individual $z \sim 1.5$ galaxies at large radii with KMOS. In this section, we provide an overview of the sample selection and its properties in the context of the parent star-forming population at similar redshift. We also describe the observations and key aspects of the data reduction for the subset of galaxies presented in this paper, corresponding to half of the sample. A similar observing strategy and data reduction will be applied to the full sample that will be presented in a forthcoming paper.

2.1 Sample selection and galaxy integrated properties

KURVS aims at obtaining ultra-deep spatially resolved observations of the Hα + [N II]$_{6548,\,6583}$ kinematics in star-forming galaxies at $z \sim 1.5$ by exploiting the multiplex capabilities of KMOS, which allows us to obtain integral field observations for up to 24 galaxies simultaneously. Therefore, the target galaxies have been selected to be located within the $7\farcs2 \times 7\farcs2$ KMOS patrol field, in order to be observed within a single KMOS pointing. In addition, the targets have been selected to lie within the Cosmic Assembly Near-infrared Deep Extragalactic Legacy Survey (CANDELS; Grogin et al. 2011) fields, to ensure access to high resolution multiwavelength photometry from *HST*, as well as low-resolution multiwavelength photometry from the ultra-violet to the near-infrared for the full sample. The final sample consists of 44 galaxies with existing Hα detections split in two KMOS pointings, with 22/44 objects in the Chandra Deep Field South (CDFS) field and 22/44 objects in the Cosmological Evolution Survey (COSMOS) field. Out of these, 35 galaxies (20/22 in CDFS and 15/22 in COSMOS) have been selected from the KMOS Galaxy Evolution Survey (KGES; Gillman et al. 2020; Tiley et al. 2021) among galaxies with pre-existing Hα detections and spatially resolved kinematics. The remaining two galaxies within CDFS and the seven COSMOS targets have been selected from the KMOS^{3D} survey (Wisnioski et al. 2019) to fully populate the KMOS arms. One of the COSMOS sources is undetected due to an incorrect spectroscopic redshift, yielding a final sample of 43 galaxies.

KURVS galaxies have spectroscopic redshifts $1.23 \leq z_\mathrm{spec} \leq 1.71$, with a median redshift $z_\mathrm{spec} = 1.50$. Integrated measurements of stellar masses, $M_\star$ and star formation rates, SFR, are fully described in Gillman et al. (2020), and we briefly report details of the adopted procedure below. The same procedure has been applied to the galaxies not included in the original KGES sample. Stellar masses and star formation rates are measured by fitting the UV-to-near-IR spectral energy distribution (SED) from the CDFS and COSMOS photometric catalogues (Guo et al. 2013; Muzzin et al. 2013) with MAGPHYS (da Cunha, Charlot & Elbaz 2008; da Cunha et al. 2015). Galaxies in the KURVS sample span a stellar mass range $\log(M_\star/\mathrm{M}_\odot) = 9.2$–$11.5$, with a median $\log(M_\star/\mathrm{M}_\odot) = 10.2^{+0.5}_{-0.4}$. Star formation rates cover a range SFR = 5–143 $\mathrm{M}_\odot\,\mathrm{yr}^{-1}$, with a median SFR $= 22^{+19}_{-9}$ $\mathrm{M}_\odot\mathrm{yr}^{-1}$. Here, the uncertainties indicate the 16$^{\mathrm{th}}$ to 84$^{\mathrm{th}}$ percentile range of the distribution. We obtain stellar continuum half-light radii, R_eff, and axial ratios, b/a, from the van der Wel et al. (2014) catalogue. These are based on *HST*-F125W imaging at $\lambda_\mathrm{obs} \sim 1.25\,\mu$m if the redshift of the source is $z_\mathrm{spec} \leq 1.25$, and on F160W imaging at $\lambda_\mathrm{obs} \sim 1.6\,\mu$m otherwise. The targets have half-light radii in the range $R_\mathrm{eff} = 1.1$–14 kpc with a median $R_\mathrm{eff} = 3.7^{+1.9}_{-1.2}$ kpc. Inclinations for the stellar continuum are measured from the b/a axial ratio, assuming a thick disc with intrinsic thickness $q_0 = 0.2$ (see equation 3 in Gillman et al. 2020, and references therein). We measure inclinations for the star-forming disc on *HST*-F814W images sampling the rest-frame UV emission in our sources by adopting a consistent procedure to that applied on near-infrared images. Measurements of these quantities for KURVS-CDFS galaxies discussed in this work are reported in Table 1.

To identify candidate active galactic nuclei (AGN) in the CDFS sample, we use the same AGN identification scheme adopted for the full KGES sample, which is based on the integrated [N II]/Hα ratio and emission-line width, as well as infrared colours and X-ray luminosities (see Gillman et al. 2022 for details on the procedure). Of the 22 sources in the KURVS-CDFS sample, we identify two galaxies (KURVS-11 and KURVS-12) whose infrared colours indicate the presence of an AGN. KURVS-12 also has a X-ray counterpart and an intrinsic 0.5–7.0 kev luminosity of $L_\mathrm{X\text{-}ray,\,int} = 5 \times 10^{42}\,\mathrm{erg\,s^{-1}}$ in the Luo et al. (2017) catalogue, which also supports the presence of an AGN. Three other galaxies in the sample have X-ray counterparts but luminosities that lie below the AGN threshold. These objects likely hosting an AGN do not show highly perturbed velocity or velocity dispersion maps, hence we do not exclude them from our analysis.

Owing to the adopted selection criteria mainly based on their projected sky distribution, KURVS galaxies are a representative subset of spectroscopically-selected $z \sim 1.5$ galaxies with $\log(M_\star/M_\odot) \sim 10$. This is demonstrated in Fig. 1, showing the distribution of KURVS with respect to KGES galaxies in the stellar mass versus star formation rate plane (left), and in the stellar mass versus half-light radius plane (right). Fig. 1 also shows that the ∼70 per cent of KURVS galaxies are located within a factor of 4 of the main sequence at $z \sim 1.5$ (Schreiber et al. 2015) and within the scatter of the stellar mass-size relation for $z \sim 1.25$–1.75 discs (van der Wel et al. 2014). Therefore, their star formation rate and structural properties suggest that KURVS galaxies are representative of $z \sim 1.5$ star-forming discs at $\log(M_\star/M_\odot) \sim 10$ and $\log(\mathrm{sSFR/yr^{-1}}) \sim -9$.

2.2 Observations and data reduction

Observations for the KURVS-CDFS pointing were carried out between 2018 October and 2019 December with the H-band filter, to detect the Hα + [N II] emission lines at $z \sim 1.5$. For this subset of the sample, 22 out of the 24 KMOS arms have been allocated to target galaxies, whilst one arm has been allocated to a star, in order to monitor the point spread function (PSF) of the observations, and to allow accurate centring of the individual frames during the data reduction process (see below). Observations were carried out with an ABAABA observing scheme, where 'A' represents the science exposure and 'B' the sky frame, respectively. Each individual exposure lasted 600 s. A total of 418 frames have been considered to reconstruct the final science cubes, while 73 frames have been discarded due to poor seeing conditions to avoid degrading the spatial resolution of the science cubes. These 'poor seeing' frames have been derived by inspection of the PSF of the standard star observed simultaneously with the science targets. The total exposure time on-source for KURVS-CDFS observations is 69.7 h, with an average seeing full width half maximum (FWHM) of $0\farcs57$.

Data cubes for each individual KMOS frame have been reconstructed using the ESO Recipe Execution Tool (ESOREX, ESO CPL Development Team 2015) pipeline, which performs standard dark,

Downloaded from https://academic.oup.com/mnras/article/524/2/2814/7221661 by University of Durham user on 31 October 2023

Table 1. Integrated properties of KURVS-CDFS galaxies.

KURVS ID	CANDELS ID	RA	Dec.	$z_{\rm spec,\,H\alpha}$	$\log(M_\star)$	*SFR*	$R_{\rm eff}$	$i_\star$	$i_{\rm SFR}$
		hh:mm:ss	dd:mm:ss		$\log(M_\odot)$	$M_\odot\,yr^{-1}$	kpc	deg	deg
(1)	(2)	(3)	(4)	(5)	(6)	(7)	(8)	(9)	(10)
1	cdfs_24904	03:32:17.35	−27:53:52.83	1.359	9.76	36	1.1 ± 0.1	39 ± 5	44 ± 5
2	cdfs_26404	03:32:15.00	−27:53:02.37	1.360	9.88	12	8.0 ± 0.9	49 ± 6	48 ± 6
3	cdfs_26954	03:32:22.10	−27:52:44.95	1.541	10.64	34	4.2 ± 0.5	43 ± 5	42 ± 5
4	cdfs_27318	03:32:20.18	−27:52:38.34	1.552	10.34	62	3.8 ± 0.4	43 ± 5	53 ± 6
5	cdfs_28138	03:32:13.78	−27:52:02.73	1.518	10.12	33	3.2 ± 0.4	57 ± 7	53 ± 6
6	cdfs_29207	03:32:14.05	−27:51:24.40	1.221	10.61	35	2.9 ± 0.3	55 ± 6	63 ± 7
7	cdfs_29589	03:32:11.23	−27:51:07.10	1.518	10.24	14	4.5 ± 0.5	78 ± 9	78 ± 9
8	cdfs_29831	03:32:06.83	−27:50:55.37	1.540	9.58	18	2.5 ± 0.3	56 ± 6	68 ± 8
9	cdfs_30267	03:32:21.52	−27:50:40.53	1.540	10.12	10	5.0 ± 0.6	50 ± 6	48 ± 5
10	cdfs_30450	03:32:29.92	−27:50:31.91	1.390	9.89	4	1.9 ± 0.2	73 ± 8	72 ± 8
11	cdfs_30557	03:32:34.03	−27:50:28.82	1.384	10.68	142	5.9 ± 0.7	68 ± 8	73 ± 8
12	cdfs_30561	03:32:31.54	−27:50:28.68	1.613	11.52	38	6.5 ± 0.8	60 ± 7	56 ± 6
13	cdfs_30732	03:32:12.50	−27:50:20.59	1.334	9.62	39	3.4 ± 0.4	39 ± 5	42 ± 5
14	cdfs_30865	03:32:37.37	−27:50:13.62	1.389	9.68	30	2.5 ± 0.3	59 ± 7	50 ± 6
15	cdfs_31127	03:32:16.94	−27:50:04.06	1.613	10.07	43	3.8 ± 0.4	65 ± 7	38 ± 4
16	cdfs_31671	03:32:37.10	−27:49:40.94	1.569	10.16	25	3.9 ± 0.5	76 ± 9	73 ± 8
17	cdfs_31721	03:32:11.12	−27:49:38.41	1.353	9.55	17	2.4 ± 0.3	42 ± 5	42 ± 5
18	cdfs_33014	03:32:32.64	−27:48:48.72	1.341	9.82	17	3.2 ± 0.4	55 ± 6	51 ± 6
19	cdfs_33246	03:32:19.79	−27:48:39.12	1.357	10.23	18	2.1 ± 0.2	39 ± 5	42 ± 5
20	cdfs_35213	03:32:25.03	−27:47:18.18	1.356	10.02	63	1.2 ± 0.1	19 ± 2	27 ± 3
21	GS4_10784	03:32:31.43	−27:51:37.48	1.382	10.17	21	2.8 ± 0.3	54 ± 6	54 ± 6
22	GS4_16960	03:32:37.74	−27:50:00.39	1.618	11.12	101	4.1 ± 0.5	38 ± 4	38 ± 4

Note. (1) Galaxy ID from KURVS; (2) galaxy CANDELS ID (Grogin et al. 2011); (3) and (4) galaxy coordinates; (5) spectroscopic redshift from the Hα emission line; (6) stellar mass from MAGPHYS. The typical uncertainty associated with this quantity is ± 0.2 dex (Mobasher et al. 2015); (7) star formation rate mass from MAGPHYS SED-fitting. The typical uncertainty associated with this quantity is ± 0.1 dex; (8) effective radius for the stellar component from van der Wel et al. (2014); (9) inclination for the stellar disc from van der Wel et al. (2014); (10) inclination for the star-forming disc from *HST*-F814W images. Quoted errors for the effective radius and inclination correspond to a typical 0.05 dex uncertainty following van der Wel et al. (2012).

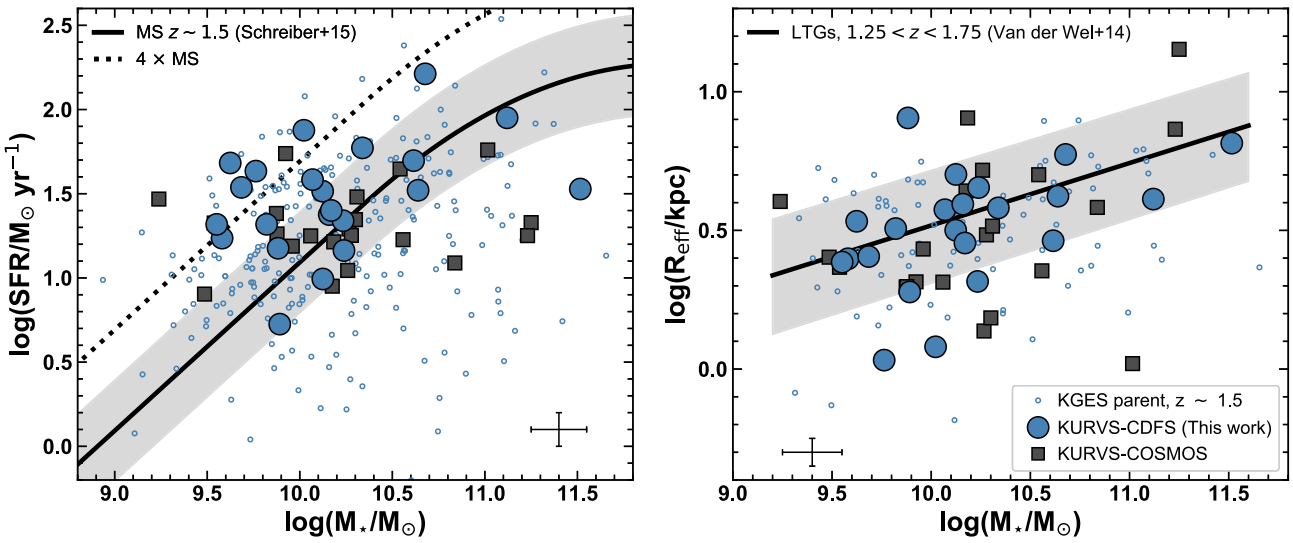

Figure 1. *Left:* Star formation rate as a function of stellar mass for our sample. Here, the star formation rate of each galaxy is normalized to the SFR of the main sequence at $z \sim 1.5$, to account for the redshift evolution of the main sequence normalization (e.g. Sargent et al. 2012). The blue filled circles correspond to KURVS galaxies in the CDFS field discussed in this work. Grey filled squares indicate KURVS galaxies in COSMOS, which will be presented in a forthcoming paper. Blue hollow circles show the parent sample from the KGES survey (Tiley et al. 2021). The median error bar for the KURVS and KGES points is shown in the bottom right. The solid line and shaded area indicate the position of the main sequence and its ±0.3 dex scatter from Schreiber et al. (2015) at $z = 1.5$, corresponding to the average redshift of the KURVS sample. The dashed line represents the factor of four threshold above which galaxies are usually classified as 'starbursts'. *Right:* Stellar half-light radius as a function of stellar mass for the KURVS sample. The median error bar for KURVS and KGES galaxies is shown in the bottom left figure. The black line and shaded area indicate the mass-size relation and its scatter at $1.25 < z < 1.75$ from van der Wel et al. (2014). KURVS galaxies are located within the main-sequence and mass-size relations at the same redshift. Therefore, their star formation rate and structural properties suggest that KURVS galaxies represent typical star-forming systems at $z \sim 1.5$.

Downloaded from https://academic.oup.com/mnras/article/524/2/2814/7221661 by University of Durham user on 31 October 2023

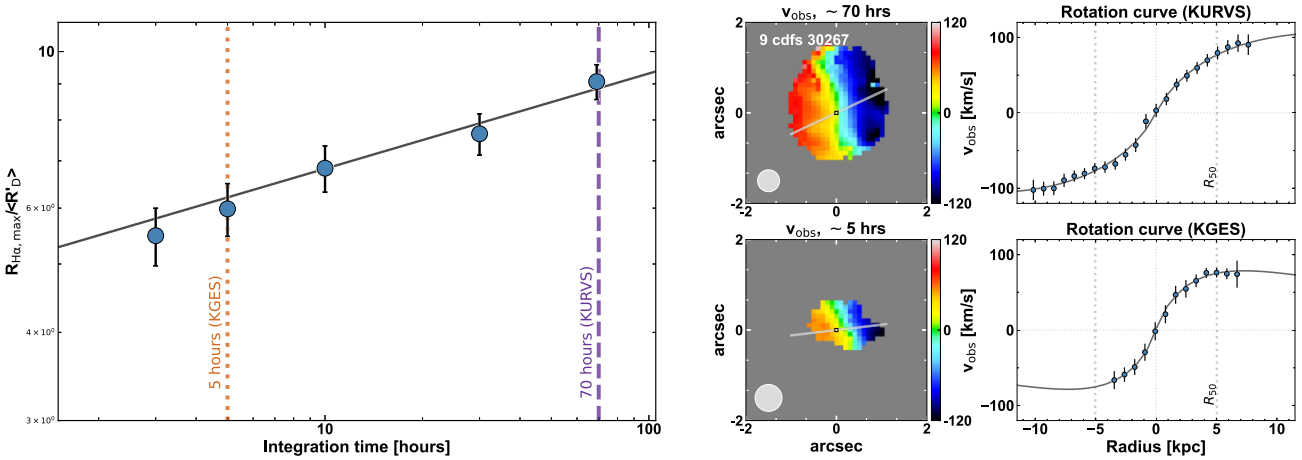

Figure 2. *Left:* Average radial extent of the Hα emission in KURVS galaxies as a function of integration time. Filled circles indicate the median extent of the Hα emission, derived as the square root of the area in which the Hα emission is detected with S/N$_{H\alpha} \geq 5$. The error bars highlight the 1σ scatter of the distribution. Coloured vertical lines highlight the typical integration time of the parent sample from the KGES survey (dark orange) and KURVS (dark purple). For 70 h of on-source integration, corresponding to the integration time in the KURVS survey, we robustly sample galaxy rotation curves out to $\sim R_{6D}$ for the average system. *Right:* example of the velocity field and rotation curve from KURVS (top row) and KGES (bottom row) observations for the same galaxy. These are measured from KMOS data cubes with a total on-source exposure time of ~70 and ~5 h, respectively, as described in Section 3. The deep observations from KURVS allow us to measure high-quality velocity maps and rotation curves extending further out into the galaxy disc, as well as to derive the dynamical centre with higher accuracy than pre-existent, shallower observations from KGES.

flat, and wavelength calibrations, and produces a 0.2 arcsecs paxel data cube for each frame. After the cube reconstruction, the sky has been subtracted from each frame. First, ESOREX has been used to perform a simple A–B subtraction. Subsequently, the Zurich Atmospheric Purge tool (ZAP; Soto et al. 2016) has been applied to each sky-subtracted cube to remove residual contamination from the sky. The frames have been flux-calibrated by using corresponding observations of the standard star taken with the target galaxies observations. Finally, to produce the stacked science cubes the calibrated frames have been centred using the position of the standard star.

The long integration of KURVS observations is critical to probe the outer regions of galactic discs at high-redshift. This is demonstrated in Fig. 2, showing the average radial extent of the Hα emission as a function of integration time, and a comparison between the velocity field and rotation curves obtained from KURVS and KGES observations, the latter having a total on-source exposure time of ~5 h, on average (Tiley et al. 2021). KGES observations allow us to recover the inner velocity field and velocity gradient of $z \sim 1.5$ galaxies, as exemplified by the right-hand panel of Fig. 2. KGES observations slightly overestimate the circular velocity at the effective radius of KURVS-CDFS galaxies by 0.2 dex, on average, and show no significant systematics for measurements of the velocity dispersion when this is measured consistently as the median of the full velocity dispersion profile in both data sets. At the same time, kinematic parameters measured from KGES observations are associated with larger error bars, and overall KURVS and KGES measurements are consistent within the 1σ uncertainties. However, shallow observations from KGES require extrapolation of the rotation curve at large radii, and this results in significant uncertainties in measurements of the outer disc kinematics. In fact, our previous analysis of the large-scale dynamics of $z \sim 1.5$ star-forming galaxies was based on stacking which allowed us to improve significantly the outer rotation curve signal-to-noise ratio (modulo systematics associated with the normalization of individual rotation curves; Tiley et al. 2019b).

3 ANALYSIS

3.1 Derivation of the emission line maps

The systemic redshift of each source has been measured from one dimensional spectra obtained by collapsing the cube in a pseudo-circular aperture with a 1.″2 diameter, to maximize the signal to noise of the Hα emission, S/N$_{H\alpha}$. The Hα + [N II]$_{6548,\,6583}$ complex and underlying continuum emission in these spectra has been modelled using a χ^2 minimization procedure that uses three Gaussian profiles and a constant function. To account for increased noise near the sky emission lines, a weighting scheme corresponding to 1/sky^2 has been applied, where 'sky' is the sky spectrum from the KMOS data reduction pipeline. The three emission lines have a common width and a fixed relative position. Furthermore, the [N II]$_{6583}$/[N II]$_{6548}$ ratio is fixed to the theoretical value of 2.96. The width and position of the emission line complex, as well as the normalization of the continuum, are free parameters of the fit. Systemic redshifts measured on KURVS spectra are in excellent agreement with pre-existent measurements from KGES (within 1 per cent).

Each spaxel was re-sampled from the native 0.″2 spaxel^{-1} resolution to a 0.″1 spaxel^{-1} scale, conserving the flux in each slice during the process. An adaptive binning procedure has been applied to the cubes, similarly to that applied in the analysis of data in the KROSS and KGES surveys (Stott et al. 2016; Tiley et al. 2019b, 2021). For each spaxel, the flux is averaged in an increasing number of spaxels until S/N$_{H\alpha} \geq 5$. Initially, each spaxel is collapsed in a ±1 spaxel radius (resulting in a 3 × 3 spaxel). If the S/N$_{H\alpha}$ of the resulting spaxel is below the S/N$_{H\alpha} = 5$ threshold, the collapsing radius is iteratively increased by one pixel up to a maximal bin radius of 4 (corresponding to a 9 × 9 spaxel) until S/N$_{H\alpha} \geq 5$. If the S/N$_{H\alpha}$ is still below the threshold, the Hα emission at that spaxel is considered undetected and the corresponding spaxel is masked in the final data cube.

The Hα + [N II]$_{6548,\,6583}$ spatially resolved emission is modelled by applying the same procedure used to fit the one-dimensional spectra to each spaxel in the binned data cube. To minimize contamination

Downloaded from https://academic.oup.com/mnras/article/524/2/2814/7221661 by University of Durham user on 31 October 2023

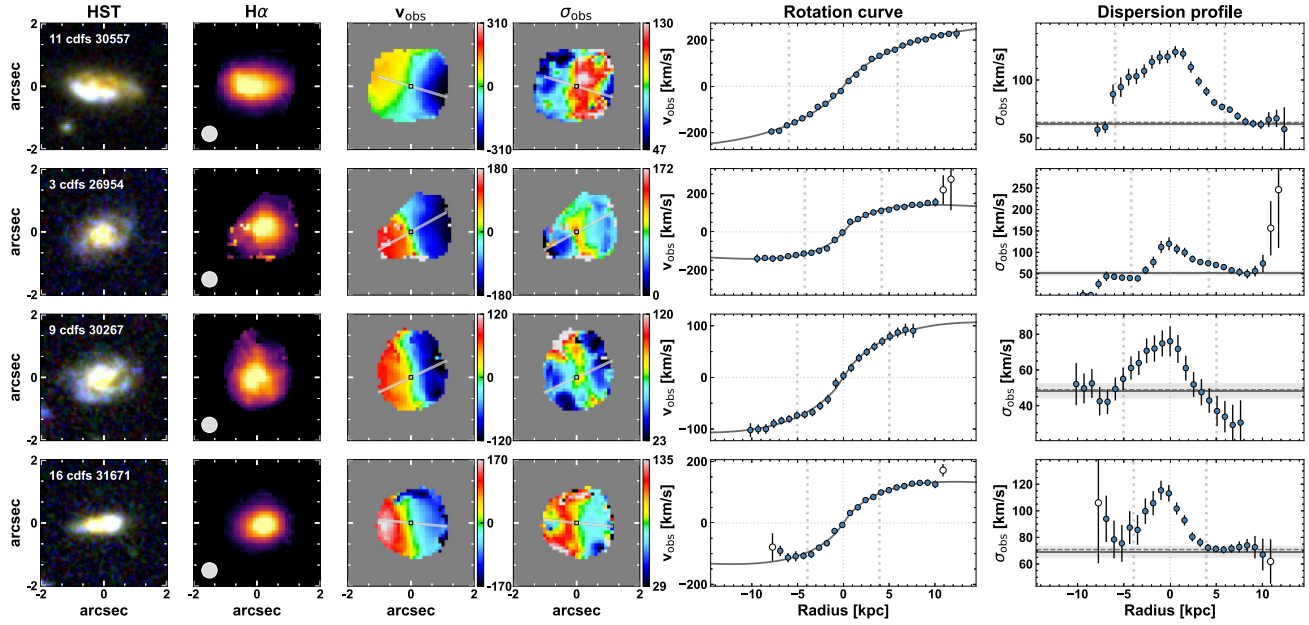

Figure 3. The KURVS data set. From left to right, the panels show the *HST* $B_{435} - z_{850} - H_{160}$ composite image, the Hα flux map, the line-of-sight velocity ($v_{\rm obs}$) and velocity dispersion ($\sigma_{\rm obs}$) maps, and the observed Hα rotation curve and velocity dispersion profile. These are extracted from the KURVS velocity and velocity dispersion maps along the kinematic major axis, indicated with a grey solid line in each map. Rotation curves are plotted such that the velocity gradient is always positive. This is achieved by multiplying the velocities by -1 where necessary, and as a result the values of the one-dimensional velocity and velocity dispersion profiles do not correspond to each other in some cases. Note that, the colour scale in the velocity and velocity dispersion maps might differ from the range of velocities of the one-dimensional profiles since it is optimized to the range of velocities and velocity dispersions measured in two-dimensional data. The size of the PSF of KURVS observations is indicated by a grey filled circle in the bottom left of each Hα flux map. The white filled circles in the rotation curves and dispersion profiles indicate pixels that have been clipped due to either a large contamination from sky lines or broad components (see the text for details). Here, the thick dotted vertical lines mark the half-light radius measured from *HST* observations (R_{50}) for reference. The black solid curve in each rotation curve plot shows the best-fitting exponential disc model to the data. For the dispersion profiles, the dotted grey and solid grey horizontal lines represent the observed and beam smearing corrected measure of the intrinsic dispersion, σ_0. The grey shaded area highlights the 1σ error of this quantity. The depth of KURVS observations allows us to probe the rotation curves of $z \sim 1.5$ star-forming galaxies out to $\gtrsim$10 kpc, well beyond the stellar effective radius, hence providing important observational constraints on the amount of baryonic and dark matter in their outer discs.

from any residual sky lines, the width of the emission lines is imposed to be wider than that of the sky lines. This is particularly relevant in regions with low S/N$_{\rm H\alpha}$ such as the outer regions of the galaxy disc. Maps for the Hα flux, [N II]$_{6583}$ flux, observed line-of-sight velocity and observed velocity dispersion are constructed from the best-fitting spatially resolved model to the observed emission. For this, the integral below the Hα component, the integral of the [N II]$_{6583}$ emission line, the position of the Hα emission line centroid relative to the systemic emission line centroid from the integrated spectrum, and the width of the emission lines are considered at each spaxel, respectively. Finally, the velocity dispersion is corrected for the instrumental broadening measured from the width of the sky emission lines. Uncertainties associated with each map are the 1σ errors obtained from the χ^2 minimization routine. At this stage, additional shifts have been applied to recentre the spatially resolved maps to account for the different morphology of the continuum and Hα emission due to the presence of star-forming clumps and/or differential dust attenuation effects. The additional shifts are computed by fitting a two-dimensional Gaussian profile to the Hα flux maps. The average shift along the x-axis is $x_{\rm shift} \sim -0\farcs03$, while along the y-axis is $y_{\rm shift} \sim -0\farcs04$. Fig. 3 shows an example of the Hα flux map, the observed line-of-sight velocity and observed velocity dispersion maps for a subset of the KURVS-CDFS galaxies. The full KURVS-CDFS sample is shown in Appendix A.

3.2 Kinematic position angles, rotation curves, and velocity dispersion profiles

To extract rotation curves and velocity dispersion profiles and hence characterize the dynamic properties of the sample, we must identify the kinematic major axis of a galaxy corresponding to the axis that maximizes the velocity gradient in the velocity map. We measure the position angle of the kinematic major axis by rotating the observed velocity map in one degree increments. At each step, we measure the median velocity in a pseudo-slit of 5 pixels (i.e. $0\farcs5$) radius along the centre of the map, derived as discussed in the previous section. To minimize the impact of noise on measurements of the position angle, we smooth the velocity gradient as a function of angle curve. We then define the position angle of the kinematic major axis as the average between the angle that maximizes the velocity gradient along the pseudo-slit and the angle that minimizes it plus 90°. We visually inspect the data to confirm that the average between the two independent measurements of the position angle corresponds to the direction of the maximum velocity gradient in the velocity maps. The measurements agree within ±5° with few notable exceptions corresponding to sources in which the velocity gradient is not well defined as a result of low inclination and/or a perturbed velocity field. This suggests that our measurements of the position angle are robust against deviations from circular motions such as inflows or outflows, which are likely to occur along the minor axis.

Downloaded from https://academic.oup.com/mnras/article/524/2/2814/7221661 by University of Durham user on 31 October 2023

We extract the rotation curve along the kinematic major axis as the median velocity at each (radial) pixel within a pseudo-slit of 3 pixels (i.e. 0.″3) radius, roughly corresponding to the 1σ width of the seeing in KURVS observations ($\sim$0.″25). To measure errors on the extracted rotation curve, we vary the observed velocity at each pixel within the pseudo-slit within the 1σ errors 1000 times and we take the standard deviation of the simulated velocity values at each pixel. We apply a similar procedure to the velocity dispersion maps to extract the velocity dispersion profile along the kinematic major axis. The last two panels of Fig. 3 show an example of the extracted rotation curves and velocity dispersion profiles for four of the KURVS-CDFS galaxies. The full sample is shown in Appendix A.

3.3 Kinematic parameters

3.3.1 Rotational velocities

In order to quantify the amount of ordered motions in each galaxy, we measure the rotation velocity at different radii. We measure observed rotational velocities in our galaxies from best-fitting models to the rotation curves derived in the previous section. This is to minimize the impact of noise and to extrapolate the measurements where the data do not extend far out enough in the galaxy disc. To parametrize each one-dimensional rotation curve, we fit it with an exponential disc model (Freeman 1970) of the form

$$(v(r) - v_{\rm off})^2 = \frac{(r - r_{\rm off})^2 \pi G \mu_0}{h}(I_0K_0 - I_1K_1), \quad (1)$$

where μ_0 and h are, respectively, the peak mass surface density and the disc scale radius, and $I_{\rm n}$, $K_{\rm n}$ are the Bessel functions evaluated at $0.5rh^{-1}$. We also allow for a systematic radial and velocity offsets, $r_{\rm off}$ and $v_{\rm off}$, respectively. While a razor thin disc model may not be a good approximation for high-redshift star-forming galaxies, which mostly present thick and turbulent discs (Förster Schreiber & Wuyts 2020, and references therein), the Freeman (1970) model provides a good fit to the observed rotation curves, and it is used here only to interpolate the observational data-points and for extrapolating the rotation curve at large radii.

We measure the observed rotation velocity at different radii from the best-fitting centred exponential disc model. To account for the impact of the seeing, we measure 'KMOS radii' R' by convolving the radius measured on *HST* observations with the 1σ-width of the seeing in KURVS observations, following Tiley et al. (2019b). To measure 1σ uncertainties on the observed rotation velocity, we resample each data point in the observed rotation curve and the relevant radii 1000 times within the 1σ errors, we fit each of these 'mock' rotation curves and we measure 'mock' observed rotational velocities. Finally, we consider as 1σ error the standard deviation of these 'mock' rotation velocity values. We note that measurements of the rotation velocity are extrapolated from the best-fitting model when the observed data do not extend far out into the disc. For most sources, this corresponds to a small extrapolation, and a comparison with the position–velocity diagrams show that the best-fitting model agree very well with the observed kinematics up to very large radii (see Fig. A4 in Appendix A). After visually inspecting the rotation curves and position–velocity diagrams, we clip a small number of non-physical pixels in six objects, where these are either affected by residual contamination from sky lines or emission from broad lines.

To obtain intrinsic measurements of rotational velocities and intrinsic velocity dispersion in the 'inner disc', i.e. within 3.4 times the disc scale radius $R'_{\rm 3.4D}$ or 2 times the effective radius, we apply a beam-smearing correction by using the prescriptions provided by Johnson et al. (2018). Since the impact of beam smearing decreases as a function of galactocentric radius (see e.g. fig. 2 in Johnson et al. 2018), we assume that the beam smearing correction is negligible in the outer disc, and we do not apply beam smearing corrections for kinematic parameters computed beyond $R'_{\rm 3.4D}$. We further correct the rotation velocity for inclination by considering the inclination measured on *HST*-F814W images sampling the rest-frame UV emission of our sources, and hence, the star formation rate similarly to the Hα emission (see Section 2.1 and Table 1).

3.3.2 Ionized gas velocity dispersions

To classify the kinematics of galaxies, we also need to measure the velocity dispersion, which allows us to quantify the disordered motions in the disc. We use the velocity dispersion profile to measure the observed velocity dispersion, $\sigma_{0,\,\rm obs}$. We measure this quantity as the weighted mean of at least 3 pixels with S/N $\geq$ 3 beyond either $R'_{\rm 3.4D}$ or 2.2 times the disc scale radius, $R'_{\rm 2.2D}$. This is a compromise between considering the outermost pixels to minimize the impact of beam smearing, and averaging out a sufficient number of pixels to minimize the impact of noise. For two galaxies (KURVS-2 and KURVS-12), the measurements are not sufficiently extended and/or less than 3 pixels are available with sufficient S/N beyond $R'_{\rm 2.2D}$. In these cases, we compute $\sigma_{0,\,\rm obs}$ as the weighted mean of the full velocity dispersion profile. We finally compute the intrinsic velocity dispersion σ_0 by using the beam smearing corrections reported in table B1 of Johnson et al. (2018), which are based on the radial extent at which the velocity dispersion is measured and the velocity gradient of the galaxy.

We tested the impact of the radial extent at which the velocity dispersion is measured by comparing measurements of the velocity dispersion in the outer disc to those derived from the full velocity dispersion profile in galaxies with velocity dispersion profiles extending beyond $R'_{\rm 2.2D}$. The two measurements of velocity dispersion are in good agreement when beam smearing corrections are applied, and we measure an average ratio of 1.13 $\pm$ 0.26. This suggests that no significant systematics are introduced when the velocity dispersion is measured from the full velocity dispersion profile and beam smearing corrections are properly accounted for.

3.4 Rotational support

The ratio between the rotation velocity $v_{\rm rot}$ and the velocity dispersion σ_0 quantifies the balance between circular and turbulent motions in a galaxy, hence provides an indication of its disc properties. In the left-hand panel of Fig. 4, we plot $v_{\rm rot}/\sigma_0$ as a function of the stellar mass for KURVS-CDFS galaxies. Here, we measure the rotation velocity as the inclination-corrected velocity at 6 times the disc scale radius, $R'_{\rm 6D}$, on the rotation curve, and the intrinsic velocity dispersion σ_0 as described in Section 3.3.2. As a reference, we also add measurements for the KGES parent sample (Tiley et al. 2021). We find $v_{\rm rot}/\sigma_0 = 1.6 \pm 0.2$ with a 16$^{\rm th}$–84$^{\rm th}$ percentile range of 1.0–2.0. Fig. 4 shows that KURVS-CDFS galaxies have $v_{\rm rot}/\sigma_0$ properties representative of the KGES parent sample. All but three KURVS-CDFS galaxies have $v_{\rm rot}/\sigma_0 \geq 1$, suggesting that the majority of galaxies in our sample are rotationally supported. We use a threshold of $v_{\rm rot}/\sigma_0 \geq 1.5$ to identify rotationally supported galaxies in our sample. This is intermediate between the $v_{\rm rot}/\sigma_0 \geq 1$ cut typically applied in large dynamical surveys at high redshift (e.g. Genzel et al. 2006; Wisnioski et al. 2015, 2019; Johnson et al. 2018) and a more conservative cut

Downloaded from https://academic.oup.com/mnras/article/524/2/2814/7221661 by University of Durham user on 31 October 2023

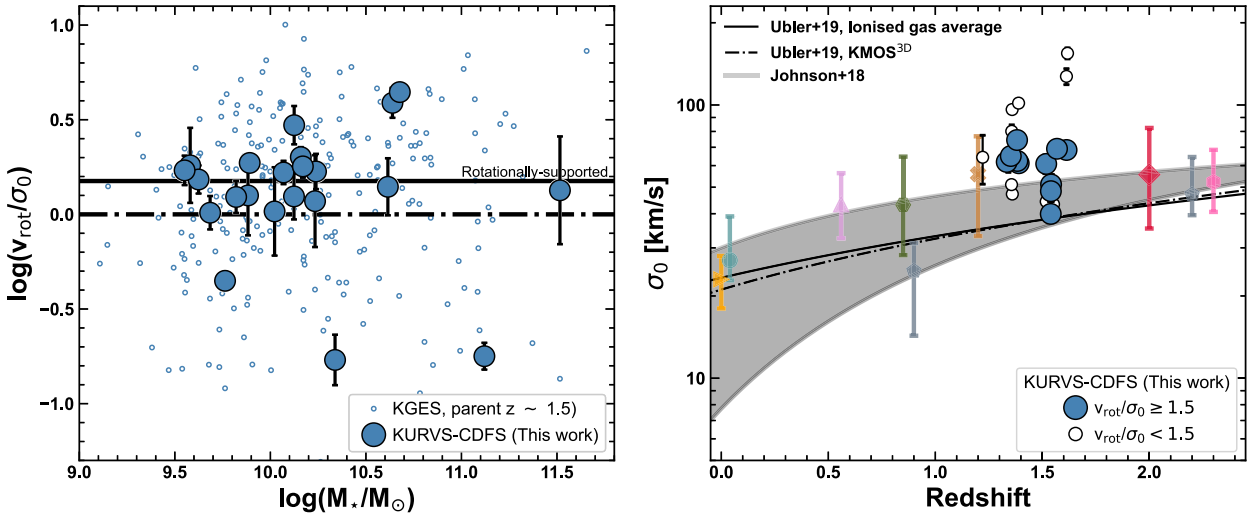

Figure 4. *Left:* Ratio between inclination corrected rotation velocity ($v_{\rm rot}$) and intrinsic velocity dispersion (σ_0) as a function of the stellar mass. The horizontal dash–dotted line marks the ratio $v_{\rm rot}/\sigma_0 = 1$, which has been used to distinguish 'dispersion dominated' ($v_{\rm rot}/\sigma_0 < 1$) and 'rotation dominated' ($v_{\rm rot}/\sigma_0 > 1$) galaxies in the literature (e.g. Wisnioski et al. 2015; Johnson et al. 2018). The horizontal solid line shows our conservative threshold $v_{\rm rot}/\sigma_0 = 1.5$ to identify rotationally supported galaxies in KURVS. The fraction of rotationally supported KURVS-CDFS galaxies is consistent with measurements of the discs fraction from KGES in a similar redshift and stellar mass range (Tiley et al. 2021). This is also consistent with KMOS^{3D} measurements when applying the same $v_{\rm rot}/\sigma_0 > 1$ cut (Wisnioski et al. 2019). *Right:* Intrinsic velocity dispersion (σ_0) as a function of redshift. Blue filled large circles and white small circles represent rotationally supported and dispersion-dominated KURVS-CDFS galaxies, respectively. The coloured symbols are literature measurements for main-sequence star-forming galaxies at different redshifts (cyan circle: SAMI; Bryant et al. 2015; orange triangle: GHASP; Epinat et al. 2010; lilac triangle: MUSE; Swinbank et al. 2017; dark grey pentagons: KMOS^{3D}; Wisnioski et al. 2015, 2019; dark green hexagon: KROSS; Johnson et al. 2018; dark yellow cross: MASSIV; Epinat et al. 2012; red diamond: SIGMA; Simons et al. 2016; pink hexagon: SINS; Cresci et al. 2009). The solid line corresponds to the fit to literature measurements of the ionized gas velocity dispersion, and the dot–dashed line is the best-fitting trend from KMOS^{3D} (Übler et al. 2019). The grey shaded area represent the redshift evolution of σ_0 for a Toomre disc instability toy model with $\log(M_\star/[{\rm M}_\odot]) = 9.8$–$10.8$ (Johnson et al. 2018), which corresponds to the 16$^{\rm th}$–84$^{\rm th}$ percentile range of the stellar mass distribution of the KURVS-CDFS sample (see Section 2.1). Rotationally supported KURVS-CDFS galaxies follow the σ_0–z trend highlighted by previous studies. Overall, the integrated dynamical properties of KURVS-CDFS galaxies suggest that these are typical $z \sim 1.5$ star-forming discs at $\log(M_\star/[{\rm M}_\odot]) \sim 10.2$.

of $v_{\rm rot}/\sigma_0 \geq 3$ which selects a strictly rotation-dominated, 'discy' sub-sample (Tiley et al. 2019a, 2021). Using this value, we find a disc fraction $f_{\rm disc} = 50 \pm 20$ per cent,[1] which is consistent with the fraction of discs measured in large integral field surveys in a similar stellar mass and redshift range (Kassin et al. 2012; Simons et al. 2016, 2017; Johnson et al. 2018; Wisnioski et al. 2019; Förster Schreiber & Wuyts 2020; Tiley et al. 2021). A visual inspection of the velocity and velocity dispersion maps, and one-dimensional velocity and velocity dispersion profiles confirms that the cut of $v_{\rm rot}/\sigma_0 \geq 1.5$ allows us to select galaxies that have regular and rotationally supported dynamics, line-of-sight velocity dispersion that peaks in the central regions and disc-like morphologies, hence representative of star-forming discs at $z \sim 1.5$.

3.5 Redshift evolution of the velocity dispersion

The right-hand panel of Fig. 4 shows the intrinsic velocity dispersion as a function of redshift for KURVS-CDFS galaxies and a compilation of measurements from the literature. This figure shows that our sample displays velocity dispersions that are overall consistent with the trend expected from the redshift evolution of this quantity. At the same time, KURVS-CDFS galaxies have higher σ_0 than the KMOS^{3D} and KROSS trends (Johnson et al. 2018; Übler et al. 2019). However, we note that these trends are derived for 'kinematic samples' including only rotation-dominated discs, as opposed to our observations which do not apply any a priori cut on the rotational support properties of galaxies.

We measure $\sigma_0 = 69 \pm 6\,{\rm km\,s^{-1}}$ with a $48 - 90\,{\rm km\,s^{-1}}$ 16$^{\rm th}$–84$^{\rm th}$ interquartile range. This is $\sim$1.5 $\times$ higher than the velocity dispersion measured in galaxies from the KGES survey at similar redshifts (Tiley et al. 2021). However, this difference can again be explained considering that Tiley et al. (2021) measurements are restricted to a 'kinematic sample' with main-sequence like SFR, spatially resolved Hα emission up to $R'_{\rm 2.2D}$ and no signs of AGN emission, which is biased against sources with high velocity dispersion. Indeed, the full KGES sample has an average velocity dispersion of $75 \pm 4\,{\rm km\,s^{-1}}$ with a 38–$101\,{\rm km\,s^{-1}}$ 16$^{\rm th}$–84$^{\rm th}$ interquartile range, and this is fully consistent with measurements of KURVS-CDFS galaxies. We therefore conclude that KURVS-CDFS galaxies have velocity dispersions overall consistent with the star-forming population at $z \sim 1.5$. The higher values than the average can be explained by a combination of the sample selection, which does not include any a priori cut on the dynamical properties of the galaxies, as well as by intrinsic variations within the galaxy population, showing substantial scatter at a given redshift (e.g. Johnson et al. 2018; Übler et al. 2019).

3.6 Outer rotation curve shapes

We begin investigating the large-scale dynamics of $z \sim 1.5$ star-forming galaxies by studying the slopes of their rotation curves at

[1] We find $f_{\rm disc} = 86 \pm 30$ per cent and $f_{\rm disc} = 10 \pm 7$ per cent when using a $v_{\rm rot}/\sigma_0$ cut of 1 and 3 respectively.

Downloaded from https://academic.oup.com/mnras/article/524/2/2814/7221661 by University of Durham user on 31 October 2023

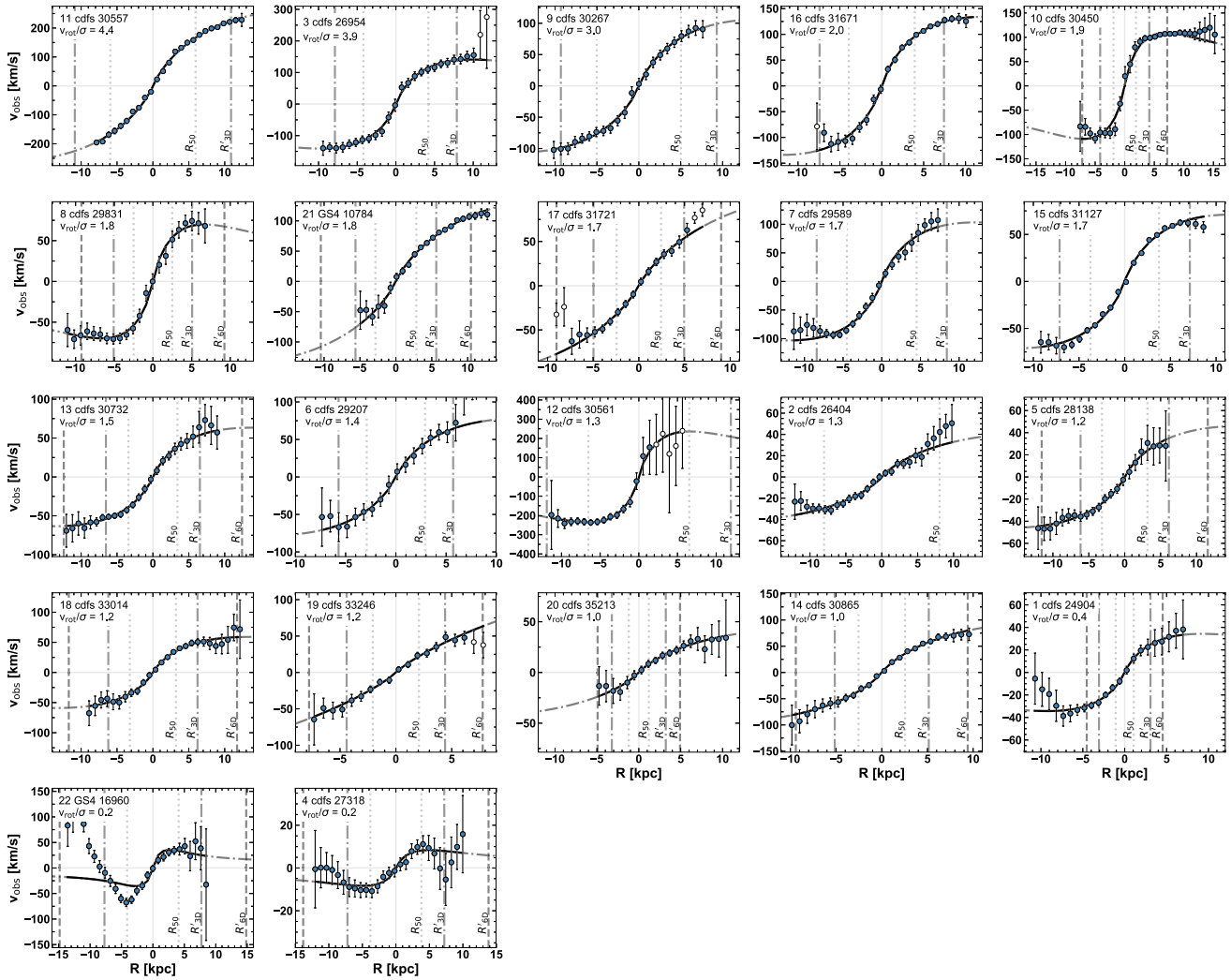

Figure 5. Rotation curves and best-fitting one-dimensional models for galaxies in the KURVS-CDFS sample. The sources are sorted in order of decreasing rotational support, quantified by the $v_{\rm rot}/\sigma$ ratio (see legend). The white circles highlight noisy or unreliable data points which have been discarded when fitting the one-dimensional kinematic model after visual inspection of the cubes and PV-diagrams. These are either contaminated by sky lines or sample broad components that do not trace the overall kinematics of the disc. The continuous black curve highlights the extent of the rotation curve that is probed by the data while the dash-dotted curve corresponds to the extrapolated model. The dotted dash–dotted and dashed vertical lines respectively mark the half-light radius measured from *HST* observations (R_{50}), and the seeing-convolved 3 × (R'_{3D}) and 6 × disc scale radii (R'_{6D}). Most galaxies have flat or rising rotation curves within R'_{6D}.

large radii. We show in Fig. 5 the rotation curves and best-fitting one-dimensional models of KURVS-CDFS galaxies. Fig. 5 shows that most rotation curves are flat or continue to rise up to $\approx R'_{6D}$.

To perform a quantitative comparison with simulations, we measure the outer rotation curve shape with the parameter $t = v_{R'_{6D}}/v_{R'_{3D}}$, following Tiley et al. (2019b). This corresponds to the ratio of the rotation velocity at R'_{6D} and that measured at R'_{3D} (≈13 and ≈7 kpc on average in our sample, see Section 3.3 and Fig. 5), roughly corresponding to the rotation velocity within and beyond the total rotation curve maximum, respectively.

A flat rotation curve would correspond to $t = 1$, whereas a rising or falling curve would be indicated by $t > 1$ and $t < 1$, respectively. Fig. 6 shows the t parameter for observed and simulated $z \sim 1.5$ galaxies as a function of stellar mass and stellar mass surface density. For consistency with the method used for observed galaxies, here we compute t parameter on individual galaxies in the EAGLE simulation, selected to have $\log(M_\star/[\mathrm{M}_\odot]) \geq 9$ at $z = 1.48$ (Schaller et al. 2015, see section 5.2.1 in Tiley et al. 2019b for how these circular velocity curves have been extracted). As already discussed by Tiley et al. (2019b), most galaxies in EAGLE have stellar masses $\log(M_\star/\mathrm{M}_\odot) \lesssim 10.3$ and display flat or rising rotation curves out to R'_{6D}. At the same time, the t parameter shows a weak correlation and increased scatter with stellar mass (left-hand panel in Fig. 6), such that a larger fraction of massive galaxies in EAGLE have declining rotation curves at large radii. The correlation appears to be stronger with the stellar mass surface density (right-hand panel in Fig. 6) and with a tighter scatter, such that most EAGLE galaxies with $\log(M_\star/R^2_{\rm eff}/[\mathrm{M}_\odot/\mathrm{kpc}^2]) \gtrsim 10$ display declining rotation curves out to R'_{6D}. EAGLE galaxies with significantly declining rotation curves ($t \leq 0.95$) are massive ($\log(M_\star/[\mathrm{M}_\odot]) \gtrsim 10$) and compact ($R_{\rm eff} \lesssim 1.3$ kpc). These are a small fraction of the full EAGLE sample considered here (6 per cent), but represent the 25 per cent of simulated galaxies beyond $\log(M_\star/[\mathrm{M}_\odot]) \gtrsim 10$. These objects have declining rotation curves at these spatial scales because this is also the scale where the galaxy transitions from

Downloaded from https://academic.oup.com/mnras/article/524/2/2814/7221661 by University of Durham user on 31 October 2023

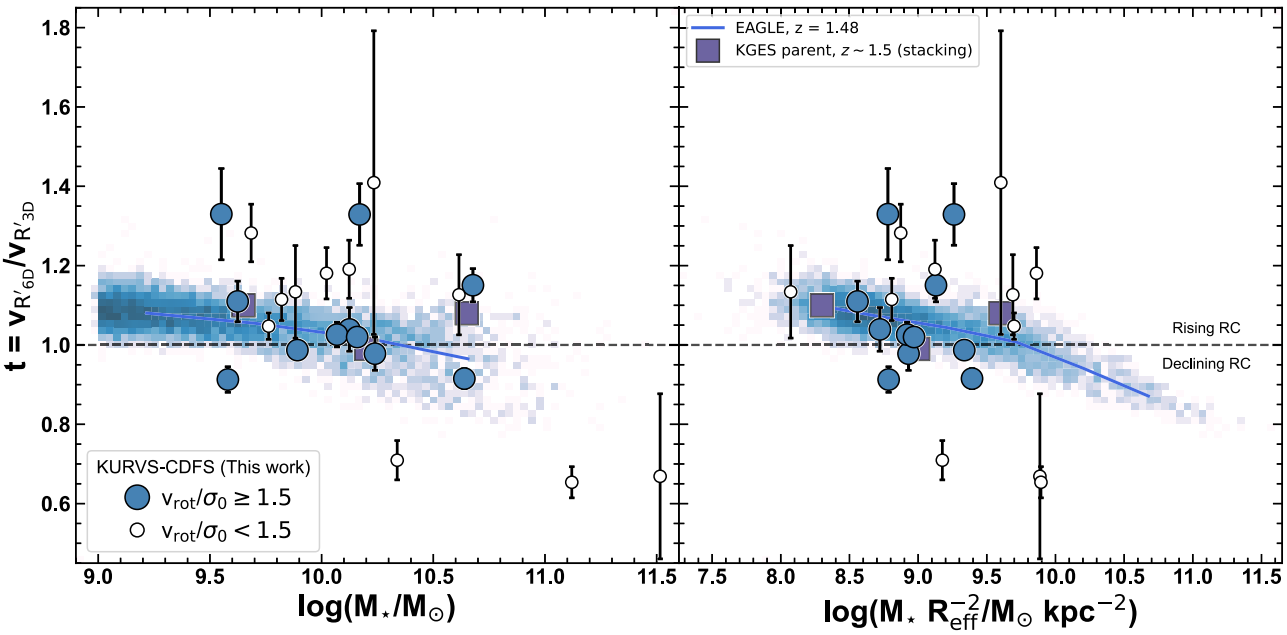

Figure 6. Outer rotation curve slope, $t = v_{R'_{6D}}/v_{R'_{3D}}$, as a function of stellar mass (left) and stellar mass surface density (right). Measurements for simulated EAGLE galaxies at $z = 1.48$ are displayed with a 2D density histogram in blue. The running median for EAGLE galaxies is shown as a blue solid line. Measurements from stacked rotation curves at $z \sim 1.5$ from the KGES survey are shown with purple squares for comparison with our previous work (Tiley et al. 2019b). Large filled blue circles and small white circles represent measurements for rotationally supported and dispersion-dominated KURVS galaxies, respectively. The majority of observed rotation curves are flat or rising out to R'_{6D}, suggesting that $z \sim 1.5$ star-forming galaxies with stellar masses $\log(M_\star/M_\odot) \sim 10.2$ contain a large fraction of their total mass in the form of dark matter within this radius. Only three objects show substantially declining rotation curves. However, these have perturbed velocity fields and are dispersion dominated. Therefore, measurements of the kinematics for such galaxies are highly uncertain. The observed rotation curve slopes are overall consistent with measurements of simulated EAGLE galaxies at similar redshifts.

being locally baryon-dominated to dark matter-dominated. These simulated galaxies present flat circular velocity curves beyond R'_{6D}. We stress here that for the simulated galaxies we use circular velocity curves, and these are not influenced by perturbed gas kinematics. This explains the tight scatter of EAGLE galaxies in Fig. 6.

Focusing on the properties of observed galaxies, three KURVS galaxies have significantly declining rotation curves at large scales. Of these, one is a massive galaxy with $v_{rot}/\sigma_0 \sim 1.3$ and a prominent bulge, as suggested by its *HST* imaging and its high Sersic index ($n_{Ser} = 2.5$). The integrated spectrum and kinematic map of this galaxy both indicate the presence of a prominent broad component ($\Delta v \gtrsim 300\,\mathrm{km\,s^{-1}}$), possibly tracing outflowing gas. This suggests that an outflow or non-circular motions might be perturbing the kinematics of this object. The other two objects have $v_{rot}/\sigma_0 \sim 0.2$ and a highly perturbed velocity field (see Appendix A). Furthermore, one of these galaxies is detected in X-rays and has an intrinsic 0.5–0.7 keV luminosity of $L_{X\text{-ray}} \approx 1.1 \times 10^{42}\,\mathrm{ergs^{-1}}$ in the Luo et al. (2017) catalogue. This galaxy is also detected in the far-infrared and has a total far-infrared luminosity $L_{IR} \approx 3 \times 10^{12}\,L_\odot$. This suggests that AGN and/or a merger-driven starburst are powering the Hα emission of this object (Birkin et al., submitted) and its kinematics are highly perturbed.

Measurements of t for KURVS-CDFS galaxies are reported in Table 2. The galaxies in our sample display overall rising rotation curve profiles at large radii, in broad agreement with the trend predicted from simulations and previous results from stacking (Tiley et al. 2019b). Our sample does not show any clear trend of declining rotation curves as a function of stellar mass or stellar mass surface density. This is, however, expected, because our galaxies probe a relatively narrow stellar mass/stellar mass surface density regime around $\log(M_\star/M_\odot) \sim 10.2$ and $\log(M_\star/R^2_{eff}/M_\odot/\mathrm{kpc}^2) \sim 9$ as a result of our selection (see Section 2.1). Fourteen galaxies have $t \sim 1$ within the 1σ uncertainty, and hence flat rotation curves within R'_{6D}, corresponding to 64 per cent of the KURVS-CDFS sample. Four sources or 14 per cent of the sample have significantly rising rotation curves ($t \geq 1.2$) and are outliers from the simulated galaxies' trend at $\gtrsim 1\sigma$. This does not seem to be associated with incorrect measurements of the disc scale radius, as this quantity is consistent with the mass–size relation in all but one of these galaxies. Furthermore, high-resolution imaging from *HST* does not show any indication of extended faint components, suggesting that current measurements of the disc scale radius are robust. Future deep observations from *JWST* will allow us to improve measurements of the baryonic disc scale radius. Four objects show declining rotation curves and $t < 1$ at $\gtrsim 2\sigma$ significance, corresponding to the 14 per cent of the sample. Three of these objects show substantially declining rotation curves, having $t \sim 0.7$, at $\gtrsim 5\sigma$ significance. These sources have dispersion-dominated dynamics and perturbed velocity fields. We therefore conclude that there is an overall good agreement between the outer rotation curve shapes of observed and simulated $z \sim 1.5$ galaxies at $\log(M_\star/M_\odot) \sim 10.2$.

We note that 12 galaxies have a rotation curve that extends up or beyond R'_{6D}, when accounting for uncertainties in this quantity. To test the robustness of our results against extrapolations of the rotation curve at large radii in the remaining of the sample, we measure the ratio $v_{R'_{6D}}/v_{H\alpha,max}$, where $v_{H\alpha,max}$ represents the velocity at the maximal extent of the rotation curve. We measure a median $v_{R'_{6D}}/v_{H\alpha,max} = 1.01^{+0.09}_{-0.07}$ where the uncertainties represent

Downloaded from https://academic.oup.com/mnras/article/524/2/2814/7221661 by University of Durham user on 31 October 2023

Table 2. Kinematic properties of KURVS-CDFS galaxies.

KURVS ID	$R_{H\alpha,\,max}$ kpc	σ_0 km s^{-1}	v_{rot}/σ_0 km s^{-1}	t
(1)	(2)	(3)	(4)	(5)
1	10.7	96 ± 2	0.4 ± 0.1	1.05 ± 0.03
2	12.1	47 ± 1	1.3 ± 0.3	1.13 ± 0.12
3	11.7	51 ± 4	3.9 ± 0.1	0.92 ± 0.03
4	12.0	43 ± 2	0.2 ± 0.1	0.71 ± 0.05
5	12.1	44 ± 3	1.2 ± 0.2	1.19 ± 0.07
6	8.1	64 ± 13	1.4 ± 0.2	1.13 ± 0.10
7	11.4	61 ± 5	1.7 ± 0.2	0.98 ± 0.04
8	11.0	40 ± 3	1.8 ± 0.4	0.91 ± 0.03
9	10.2	48 ± 4	3.0 ± 0.3	1.04 ± 0.06
10⋆	15.2	61 ± 2	1.9 ± 0.1	0.99 ± 0.02
11	12.4	62 ± 2	4.4 ± 0.2	1.15 ± 0.04
12	11.2	127 ± 9	1.3 ± 0.3	0.67 ± 0.21
13	12.1	62 ± 4	1.5 ± 0.1	1.11 ± 0.05
14	9.8	102 ± 3	1.0 ± 0.1	1.28 ± 0.07
15	9.2	68 ± 4	1.7 ± 0.1	1.03 ± 0.03
16	10.9	69 ± 4	2.0 ± 0.1	1.02 ± 0.02
17	9.9	65 ± 3	1.7 ± 0.1	1.33 ± 0.12
18	12.1	61 ± 5	1.2 ± 0.1	1.11 ± 0.05
19	7.9	80 ± 4	1.2 ± 0.2	1.41 ± 0.38
20	10.4	51 ± 2	1.0 ± 0.3	1.18 ± 0.06
21	12.7	74 ± 2	1.8 ± 0.1	1.33 ± 0.08
22	13.6	155 ± 7	0.2 ± 0.1	0.65 ± 0.04

Note.(1) KURVS ID; (2) Maximal extent of the observed rotation curve; (3) Intrinsic velocity dispersion, corrected for instrumental broadening and beam smearing (see the text for details); (4) Rotational support; (5) Outer rotation curve slope. ⋆While this galaxy displays the typical kinematics signatures of a rotating disc in KURVS observations, the *HST* imaging suggests that these are associated with the orbital motion of a merging pair (see Appendix A for details). We therefore exclude this galaxy from the dark matter fraction analysis presented in Sections 3.7 and 3.8.

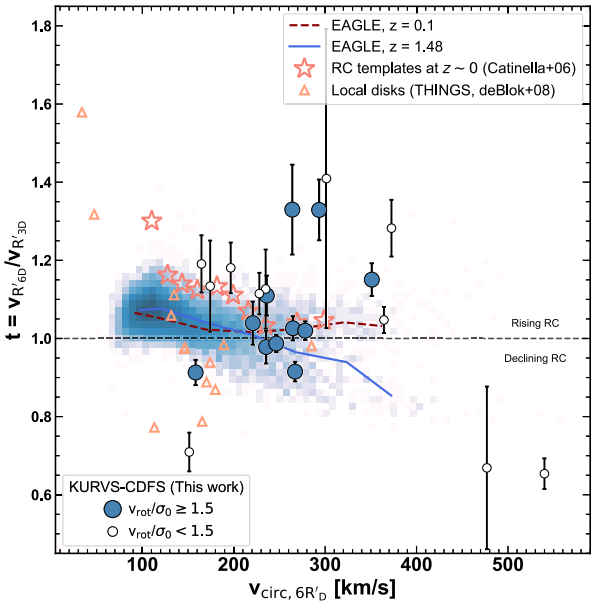

Figure 7. Outer rotation curve slope as a function of circular velocity at R_{6D} for local and high-redshift star-forming galaxies. The 2D density histogram shows measurements for simulated EAGLE galaxies at $z = 0.1$ and $z = 1.48$, with the coloured lines highlighting the running median at each redshift as specified in the legend. The colour code for KURVS-CDFS galaxies is analogous to Fig. 6. Open light-orange triangles show measurements for local discs from the THINGS survey (de Blok, McGaugh & Rubin 2001; Trachternach et al. 2008), while the open pink stars indicate the rotation curve templates of local star-forming discs from Catinella, Giovanelli & Haynes (2006). Outer rotation curve slopes of $z \sim 1.5$ star-forming galaxies are similar to measurements of local discs with similar rotational velocities suggesting little evolution with cosmic time at fixed dynamical mass.

the 16th to 84th interquartile range. This suggests a marginal effect of extrapolations on measurements of the outer rotation curve slope discussed in this section. Measurements of the rotation velocity at these relevant radii are indicated in Appendix A. To further quantify the impact of extrapolations on our conclusions, we measure the outer rotation curve slope as the ratio between the rotation velocity around R'_{4D}, which is reached by the majority of galaxies in the KURVS-CDFS sample. Measuring the outer rotation curve slope around R'_{4D} does not affect our conclusions, suggesting that our results are robust against extrapolations of the rotation curve at large radii.

We compare our measurements with the outer rotation curve shapes of local star-forming discs in Fig. 7, where we show the t parameter as a function of the circular velocity for $z \sim 1.5$ discs and local disc galaxies (de Blok et al. 2001; Trachternach et al. 2008; Catinella et al. 2006). For details on measurements of the circular velocity and t in local galaxies see Appendix B. This figure shows that local and high-redshift star-forming galaxies in a similar circular velocity regime have diverse shapes, with mostly increasing or flat rotation curves at large radii. This was already seen in the Tiley et al. (2019b) stacking analysis. This plot suggests little redshift evolution of the large-scale kinematic properties of galaxies at fixed circular velocity, similarly to what is found in simulated EAGLE galaxies and in previous studies (e.g. Harrison et al. 2017).

3.7 Inner kinematics

We now compute the dark matter fraction within the effective radius, $f_{DM}(\leq R_{eff})$, which provides indications on the processes regulating the mass assembly of galaxies as well as the interplay between baryons and the surrounding dark matter halo. We restrict this analysis to the eleven rotationally supported ($v_{rot}/\sigma_0 \geq 1.5$) KURVS-CDFS galaxies, to minimize the contribution of turbulent motion to the galaxy dynamics. Furthermore, we exclude from this analysis an interacting system of two galaxies which is unresolved with the seeing of our observations.

To measure the dark matter fraction within the effective radius, we need to subtract the contribution of baryons to the rotation curve at this radial scale. However, the effective radii of KURVS-CDFS galaxies are ∼1.5 times the size of the KMOS PSF, on average. This implies that, while the outer rotation curve slopes can be robustly recovered with minimal corrections and minimal modelling, the inner rotation curve shapes are heavily impacted by beam smearing, preventing an accurate kinematic decomposition at these small spatial scales. To correct the inner rotation curve for the effect of beam smearing, we use the GALPAK^{3D} tool (Bouché et al. 2015), which allows us to obtain an 'intrinsic' velocity field (i.e. corrected for the PSF and line spread function, LSF) by fitting a parametric model to a data cube. We adopt an exponential disc light profile with a Gaussian thickness of scale height $0.15R_{eff}$. To model the kinematics, we use a Freeman exponential disc for consistency with our analysis of the outer disc dynamics. We fit this model to the continuum-subtracted KMOS cubes. We extract rotation curves and velocity dispersion profiles from the PSF- and LSF-convolved best-fitting GALPAK^{3D} velocity and velocity dispersion maps, respectively, by applying the same method that was described in Section 3.3. We

Downloaded from https://academic.oup.com/mnras/article/524/2/2814/7221661 by University of Durham user on 31 October 2023

accept the convolved rotation curve and velocity dispersion profile that minimize the weighted χ^2 with respect to the observed profiles as the best-fitting solution. This is because we want our best-fitting solution to be driven by the dynamics of the galaxy, which can be accurately reproduced with a smooth rotating disc, as opposed to the flux distribution which is clumpy and hence difficult to model with a smooth light profile. We finally extract a 'beam smearing corrected' rotation curve from the deconvolved velocity map associated with our best-fitting solution, which we consider in the rest of the analysis presented in this section. We stress that, while forward-modelling techniques allow us to correct for the effects of beam smearing to recover the inner rotation curve shape, these models involve a large number of free parameters which can result in covariance between the best-fitting model parameters. The degeneracy and level of covariance depends on the intrinsic extent of the galaxy with respect to the seeing, its intrinsic brightness, and its Hα morphology and emission line profile. However, while fixing the inclination to the *HST* value does not affect our results, we find strong covariance between the effective radius and the inclination in most cases, and this reflects the seeing-limited nature of KURVS observations. This is expected, given that the covariance between parameters is data- and seeing-specific (Bouché et al. 2015). We therefore decide to adopt results from GALPAK^{3D} only to model the inner regions of the galaxies' discs.

Section 3.3.2 shows that turbulent motions provide a significant contribution to the dynamics of KURVS-CDFS galaxies, even when considering sources with $v_{rot}/\sigma_0 \geq 1.5$ as in this section. As a result, turbulent motions partly compensate the gravitational force, and the rotation velocity is less than the circular velocity. Hence, we must correct the 'beam smearing corrected' rotation curves for pressure support. We derive circular velocities using the Burkert et al. (2010) formalism, considering as our characteristic velocity dispersion σ_0 the value from the Hα velocity dispersion profiles (see Section 3.3 and Table 2). Here, we use observational estimates of the velocity dispersion, rather than the value output by GALPAK^{3D}, because this model does not allow us to fully capture the intrinsic complexity of the clumpy Hα flux distribution, and hence of the turbulence profile, in high-redshift discs. Future, high-resolution observations with adaptive-optics equipped integral field spectrographs such as ERIS or high spatial resolution observations with ALMA will allow us to improve our estimates of the velocity dispersion against beam smearing effects, and minimise this source of scatter in measurements of the dark matter fraction.

Finally, we model the baryonic contribution to this 'intrinsic' (i.e. corrected for the PSF, LSF, and pressure support) rotation curve with a Freeman disc with mass corresponding to the sum of the stellar mass and a 40 per cent molecular gas fraction,[2] which is the typical value expected from scaling relations at the average stellar mass and redshift of our sample (Tacconi, Genzel & Sternberg 2020). We tested however that evaluating the molecular gas fraction from the Tacconi et al. (2020) scaling relation at the stellar mass of each galaxy does not affect the results on measurements of the dark matter fraction within the effective radius. We assume that the baryonic component has an effective radius corresponding to that measured on *HST* imaging in the near-infrared. We adopt a Freeman thin disc to model the baryonic contribution to the rotation curve for simplicity. In reality, high-redshift galaxies predominantly have turbulent and clumpy discs, but more observations are needed to constrain the discs' intrinsic thickness. While the shape of the rotation curve for a thick disc is similar to that of the thin disc approximation at large radii, a disc model with intrinsic thickness $q_0 = 0.2$ would decrease the velocity of the baryonic component by ∼10 per cent at the effective radius (e.g. Casertano 1983). This is within the uncertainties for our estimated dark matter fractions at these scales, and does not affect our conclusions. A thick disc would also modify the shape of the baryonic rotation curve at radial disc scales, hence accurate modelling of this component is required to derive dark matter profiles of high-redshift galaxies. This is beyond the scope of this work, and we defer measurements of the dark matter profiles in the full KURVS sample to a future paper (Dudzevičiūtė et al. in preparation).

[2]Here we define the molecular gas fraction as $f_{mol} = M_{mol}/(M_\star + M_{mol})$

Table 3. Dark matter fraction of rotationally supported KURVS-CDFS galaxies.

KURVS ID (1)	$f_{DM}(\leq R_{eff})$ (2)
11	0.42 ± 0.09
13	0.62 ± 0.07
15	0.31 ± 0.13
16	0.50 ± 0.08
17	0.69 ± 0.06
21⋆	0.0
3	0.19 ± 0.13
7	0.46 ± 0.11
8	0.67 ± 0.06
9	0.54 ± 0.07

Note. (1) KURVS-ID. (2) Dark matter fraction within the effective radius and 1σ uncertainties. This is obtained on seeing- and pressure support- corrected rotation curves using equation (2). Galaxies are sorted in order of decreasing v_{rot}/σ_0. ⋆Galaxy KURVS-21 has a highly asymmetric velocity field, that makes it difficult to find a best-fitting model with GALPAK^{3D}. While we report its dark matter fraction for completeness, this measurements is highly unreliable and we flag this galaxy in the relevant plots.

3.8 Dark matter fraction within the effective radius

We use the beam-smearing and pressure-support corrected rotation curves to compute the dark matter fractions at the effective radius as

$$f_{DM}(\leqslant R_{eff}) = 1 - \frac{v^2_{bar}(R_{eff})}{v^2_{tot}(R_{eff})}. \quad (2)$$

Here, v_{tot} is the velocity of the pressure-support and inclination-corrected best-fitting rotation curve from GALPAK^{3D}, and v_{bar} is the baryon contribution to the rotation curve as described in the previous section. Measurements of the dark matter fraction for rotationally supported KURVS-CDFS galaxies are reported in Table 3. Uncertainties quoted here correspond to the standard deviation of the dark matter fraction measured by varying the total and baryonic rotation curves within the 1σ errors 1000 times and do not consider systematics variations in the baryon mass. Varying the baryon mass by ± 0.2 dex would imply a $\mp$ variation in the dark matter fraction, on average.

The left-hand panel of Fig. 8 shows the dark matter fraction at the effective radius as a function of stellar mass. This figure shows that $f_{DM}(R_{eff}) \gtrsim 40$ per cent in most galaxies in our sample, while two galaxies show a lower dark matter fraction. Finally, one galaxy, KURVS-21, formally has zero dark matter fraction at the effective radius. This object is a compact and massive galaxy with a prominent bulge and an asymmetric rotation curve which is difficult to reproduce accurately with GALPAK^{3D}. As a result, the dark matter fraction for this object is uncertain and we flag the measurement in the plot. Therefore, we conclude that the dark matter provides a significant

Downloaded from https://academic.oup.com/mnras/article/524/2/2814/7221661 by University of Durham user on 31 October 2023

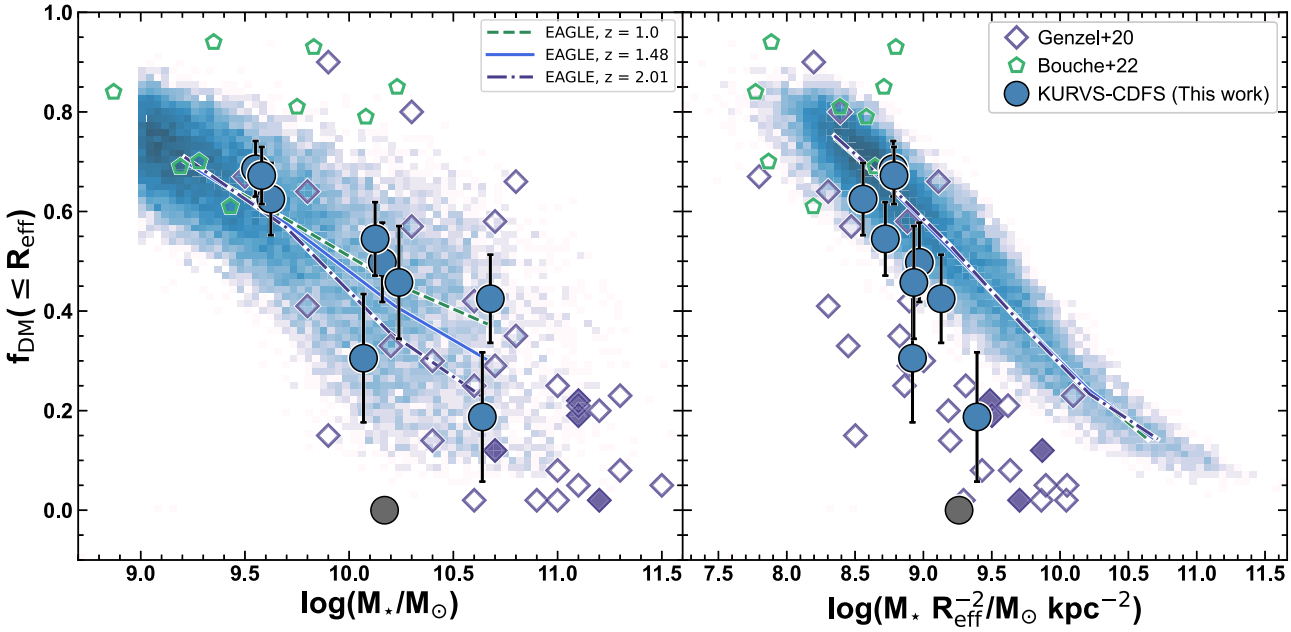

Figure 8. Dark matter fraction within the disc effective radius for high-redshift star-forming galaxies as a function of stellar mass (left) and stellar mass surface density (right). The 2D density histogram shows measurements for simulated EAGLE galaxies at $z = 1.0$, 1.48, and 2.01. The coloured lines show the running median at each redshift in EAGLE. The open green pentagons show the Bouché et al. (2022) sample of $z \sim 0.9$ star-forming galaxies. The open purple diamonds indicate the Genzel et al. (2020) sample at $0.67 \lesssim z \lesssim 2.45$, with filled symbols highlighting the sources that are in the same redshift range as our sample. Large filled circles represent rotationally supported galaxies in KURVS-CDFS, with the grey data point indicating a source whose kinematics are not well described by GALPAK^{3D}. Simulated EAGLE galaxies show a trend of decreasing dark matter fraction with increasing stellar mass, albeit with large scatter. Observed galaxies follow the same trend. There is a much tighter anticorrelation between the dark matter fraction and the stellar mass surface density in EAGLE. Observations follow a similar trend up to $\log(\Sigma_\star/M_\odot/\mathrm{kpc}^{-2}) \sim 9.2$. At higher stellar mass surface densities, however, EAGLE overpredicts the dark matter fraction of observed galaxies by a factor of ∼3.

contribution to the dynamics of rotationally supported KURVS-CDFS galaxies already at scales of the effective radius. The dark matter fraction of our sample is intermediate between that of low-mass star-forming galaxies at $z \sim 0.9$ (Bouché et al. 2022, open green pentagons in Fig. 8) and massive star-forming galaxies at $0.6 \leq z \leq 2.4$ (Genzel et al. 2020, violet diamonds in Fig. 8). Taken together, this suggests that the dark matter fraction at $R_{\rm eff}$ decreases with increasing stellar mass, as already suggested in the literature (Genzel et al. 2017, 2020; Tiley et al. 2019b; Bouché et al. 2022). This observed trend appears to be in qualitative agreement with measurements in the EAGLE simulation, which also indicate an increased scatter at stellar masses larger than $\log(M_\star/M_\odot) \sim 10.3$.

The right-hand panel of Fig. 8 shows the dark matter fraction within the effective radius as a function of stellar mass surface density. As already discussed in previous studies (Genzel et al. 2020; Bouché et al. 2022, see also Wuyts et al. 2016), this correlation is much tighter than the one with the stellar mass. The observed data agree with measurements of simulated galaxies up to $\log(M_\star R_{\rm eff}^{-2}/M_\odot kpc^{-2}) \sim 9.2$. At higher stellar mass surface density, the EAGLE simulation overpredicts the dark matter content of galaxies by a factor of ∼3–4. The low dark matter fractions measured in high-redshift galaxies with high stellar mass and stellar mass surface density have been interpreted as an indication that their inner dark matter profiles deviate from the cusps predicted in the context of ΛCDM models (Genzel et al. 2020), and other studies have also showed indications of cored dark matter profiles in lower mass galaxies in the distant Universe (Bouché et al. 2022; Sharma, Salucci & van de Ven 2022). We will explore this aspect in a future paper, using a detailed modelling of the baryonic component from spatially resolved *HST* photometry (Dudzevičiūtė et al. in preparation).

Fig. 9 shows the dark matter fraction as a function of the circular velocity at $R_{\rm eff}$ for rotationally supported star-forming galaxies at $z \sim 1.5$ and local discs. The dark matter content of $z \sim 1.5$ star-forming galaxies is similar to that of local galaxies with similar circular velocity, and it decreases as a function of this quantity. This trend seems to have little or no dependence on cosmic time.

To quantify the difference in the dark matter fraction within the effective radius between $z \sim 1.5$ and local discs, we divide the samples in two circular velocity bins and measure the average dark matter fractions in both populations. We find that $f_{\rm DM}(\leq R_{\rm eff}) = 0.57 \pm 0.16$ in KURVS galaxies with $v_{\rm circ} = 155 \pm 10\,\mathrm{km\,s^{-1}}$, and $f_{\rm DM}(\leq R_{\rm eff}) = 0.71 \pm 0.11$ in local discs from the Martinsson et al. (2013a), Martinsson et al. (2013b) sample having $v_{\rm circ} = 146 \pm 20\,\mathrm{km\,s^{-1}}$. On the other hand, we measure $f_{\rm DM}(\leq R_{\rm eff}) = 0.42 \pm 0.12$ in KURVS galaxies with $v_{\rm circ} = 221 \pm 40\,\mathrm{km\,s^{-1}}$, and $f_{\rm DM}(\leq R_{\rm eff}) = 0.57 \pm 0.23$ in local discs from the Martinsson et al. (2013a), Martinsson et al. (2013b) and Barnabè et al. (2012), Dutton et al. (2013) samples with $v_{\rm circ} = 227 \pm 40\,\mathrm{km\,s^{-1}}$. Here, the 1σ uncertainties indicate the standard deviation of the samples' distribution. That is, our measurements indicate that rotationally supported star-forming galaxies at $z \sim 1.5$ have ∼14–15 per cent lower dark matter fraction with respect to local discs with comparable circular velocities. However, this difference is less than 1σ significant and the average dark matter fractions are consistent within the 1σ uncertainties. We therefore conclude that there are no significant differences in the dark matter content of star-forming galaxies as a function of cosmic time, and that larger samples with ultra-deep

Downloaded from https://academic.oup.com/mnras/article/524/2/2814/7221661 by University of Durham user on 31 October 2023

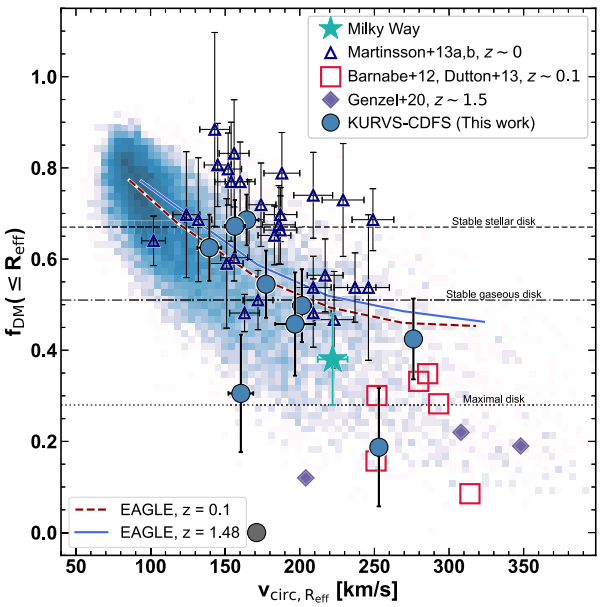

Figure 9. Dark matter fraction within the effective disc radius as a function of circular velocity at the effective radius for local and $z \sim 1.5$ star-forming galaxies. The 2D density histogram and coloured lines show measurements for simulated EAGLE galaxies at $z = 0.1$ and 1.48 as in Fig. 7. The open dark blue triangles show measurements of $z \sim 0$ spirals from Martinsson et al. (2013a, 2013b), and the filled green star indicate the dark matter fraction of the Milky Way (Bovy & Rix 2013; Bland-Hawthorn & Gerhard 2016). The open red squares indicate measurements of massive spiral galaxies with prominent bulges at $z \sim 0.1$ from the SWELLS survey (Barnabè et al. 2012; Dutton et al. 2013). The purple diamonds indicate the Genzel et al. (2020) galaxies in the redshift range of our survey. Large filled circles represent rotationally supported galaxies in KURVS-CDFS, with the grey data point indicating a galaxy whose kinematics are not well described by GALPAK^{3D}. The horizontal dotted line highlights the dark matter fraction of a maximal disc (i.e. centrally dominated by baryons) within $R_{\rm eff}$, $f_{\rm DM}(\leq R_{\rm eff}) = 0.28$. The horizontal dash–dotted and dashed grey lines show the dark matter fraction required for a gaseous and a stellar disc to be stable against axisymmetric instabilities [$(f_{\rm DM}(\leq R_{\rm eff}) = 0.51$ and $f_{\rm DM}(\leq R_{\rm eff}) = 0.67$, respectively; Efstathiou, Lake & Negroponte 1982]. The dark matter fraction of $z \sim 1.5$ discs is consistent with that of local discs in the same circular velocity interval. Therefore, this figure suggests that the dark matter content of galaxies is mostly associated with the galaxy stellar/dynamical mass with little or no trend with redshift.

observations at $z \sim 1.5$ are required for investigating systematic differences in this quantity as a function of redshift.

Our observational results are consistent with measurements of simulated EAGLE galaxies, which show the same trend of decreasing dark matter fraction as a function of the circular velocity and only a small evolution of the normalization as a function of redshift.

4 DISCUSSION AND CONCLUSIONS

In this work, we use ultra-deep observations from the KURVS survey to characterize the dynamical properties of star-forming galaxies at $z \sim 1.5$. The unprecedented depth of KURVS observations allows us measure robust rotation curve shapes out to ∼10–15 kpc, which is near or beyond 6 times the disc scale radius. Our analysis shows that most of these rotation curves are flat or rising, suggesting that dark matter dominates the dynamics of $z \sim 1.5$ star-forming galaxies at large radii, similar to discs with the same circular velocities in the local Universe and simulations (see Figs 6 and 7). We also find that, once beam smearing and pressure support are corrected for, dark matter provides a significant contribution to the dynamics of rotationally supported galaxies in our sample already within the stellar disc, again in broad agreement with measurements from cosmological simulations and in the local Universe (Figs 8 and 9). We begin this section by discussing some caveats of measurements of the dark matter fraction in the distant Universe. After that, we discuss our results in the context of literature results and simulations.

4.1 Caveats on measuring dark matter fractions in distant galaxies

Ultra-deep spatially resolved observations sampling the outer regions of the disc are an essential ingredient to characterize the outer rotation curve slope and dynamical properties of star-forming galaxies at the peak epoch of cosmic mass assembly. These observations are critical to probe the spatial scales where dark matter is expected to provide the dominant contribution to the galaxies' dynamics, and hence measure the dark matter halo mass with small extrapolations and minimal degeneracies due to the baryonic disc. At the same time, additional observational constraints on the kinematics and baryonic properties of galaxies are required to characterize the masses and density profiles of dark matter haloes in the distant Universe.

High-redshift galaxies have a highly turbulent interstellar medium, as indicated by the increase in velocity dispersion with increasing redshift (Turner et al. 2017b; Johnson et al. 2018; Übler et al. 2019; Wisnioski et al. 2019; Jiménez et al. 2022, see also the right-hand panel of Fig. 4). This implies that measurements of the circular velocity in high-redshift discs are largely dependent on the pressure-support correction, especially for low-mass galaxies that have lower rotation velocities, and at large radii, because the correction increases as a function of radius (e.g. Burkert et al. 2010). Pressure support corrections for high-redshift galaxies assume a constant characteristic value for the velocity dispersion throughout the disc, and a vertical geometry which are currently poorly constrained by data (Wellons et al. 2020, see also discussion in Bouché et al. 2022). Adaptive optics assisted integral-field observations at high spatial resolution will be needed to improve our understanding of the turbulence and vertical structure of high-redshift discs, hence improving pressure support corrections for distant galaxies. Additionally, observations of colder dynamical tracers such as the molecular gas will be important to understand the impact of feedback and outflows on measurements of the velocity dispersion, as these processes are expected to affect mostly the ionized gas component (e.g. Krumholz et al. 2018; Girard et al. 2021).

The contribution of the molecular gas to the baryon mass budget is another important aspect to consider when measuring the dark matter content of distant galaxies. Molecular gas fractions of high-redshift galaxies are substantial (perhaps up to ∼60 per cent), and there are up to a factor of ∼6 object-by-object variations (Tacconi et al. 2020). Furthermore, the molecular gas can be from ∼3 times smaller to about twice as extended as the stellar disc (Puglisi et al. 2019). Variations in the molecular gas content and extent can significantly impact measurements of dark matter fractions and profiles in distant star-forming galaxies. These effects are particularly important for the most massive and centrally concentrated galaxies, for which ALMA observations suggest ∼0.5–09 dex lower gas fractions than expected from scaling relations, and compact molecular gas cores (Tadaki et al. 2017; Elbaz et al. 2018; Franco et al. 2020; Puglisi et al. 2021). Moreover, other observational systematics, such as colour gradients reducing the stellar mass effective radius by up to a ∼25 per cent (Suess et al. 2022) or centrally peaked dust attenuation profiles (e.g.

Downloaded from https://academic.oup.com/mnras/article/524/2/2814/7221661 by University of Durham user on 31 October 2023

Tacchella et al. 2018) can impact measurements of the dark matter halo properties at high redshift, especially for the most massive star-forming galaxies. Direct observations of the molecular gas and of the stellar continuum of high-redshift discs with ALMA and *JWST* are thus needed to quantify the baryonic contribution to observed rotation curves with high accuracy, and hence dark matter fractions (e.g. Molina et al. 2019). Because these effects are expected to largely affect the most massive and centrally concentrated galaxies, i.e. the objects showing the largest discrepancies from the predictions of models, obtaining direct constraints on the full baryon profile of these galaxies might help to alleviate the tension between models and observations.

Finally, beam smearing effects impact the study of the small-scale dynamics of distant galaxies, as extensively discussed in the literature (e.g. Cresci et al. 2009; Bouché et al. 2015; Di Teodoro, Fraternali & Miller 2016). Here, we use a parametric tool to correct inner rotation curves for beam smearing, following a similar procedure to that which has been broadly applied across various studies of high-redshift galaxies (e.g. Genzel et al. 2020; Sharma et al. 2021; Price et al. 2021; Rizzo et al. 2021). On the other hand, while parametric tools are an excellent resource for recovering the galaxy kinematics at small scales for seeing-limited observation, these tools have a large number of free parameters which imply large degeneracies in the results. Higher resolution observations will be key to link the outer and small-scale kinematics of distant galaxies and study their dark matter content within the optical radius with high accuracy.

In summary, ultra-deep rotation curves are the first essential step in quantifying the dynamics of baryons and the radial distribution of dark matter in the distant Universe. However, a full sampling of the baryon mass and distribution at high spatial resolution is needed to quantify the properties of dark matter haloes at high redshift with high accuracy and quantify possible deviations between observations and theoretical models.

4.2 Comparison with $z \sim 0$ discs and simulations

Leaving aside the systematics discussed above, which are common to most observational estimates of the dark matter content of distant galaxies, we can start discussing our results in the context of other samples of local and high-redshift star-forming galaxies, as well as simulations.

Our study shows that the contribution of dark matter to the dynamics of galaxies decreases as a function of the stellar mass/stellar mass surface density, similarly to what is suggested by observations in the local Universe (Courteau & Dutton 2015). In fact, Figs 7 and 9 show that the outer rotation curve shapes and dark matter content of galaxies seem to have little evolution with cosmic time at fixed circular velocity. These observational results are in agreement with measurements of simulated EAGLE galaxies, which indicate high dark matter fractions within the effective radius in galaxies with $\log(M_\star/\mathrm{M}_\odot) \geq 9$ at nearly all redshifts up to $z \sim 2$. This is not incompatible with literature results, showing that high-redshift discs have significantly lower dark matter fractions than predicted from cosmological models (Genzel et al. 2017, 2020; Price et al. 2021). In fact, KURVS observations sample the scatter of the $z \sim 1.5$ main sequence and mass-size relation at $\log(M_\star/\mathrm{M}_\odot) \sim 10$–$10.5$ (see Fig. 1), which is close to the knee of the stellar mass function of the star-forming population in the same redshift range ($\log(M_\star/M_\odot) \sim 10.42$; Davidzon et al. 2017). On the other hand, the Genzel et al. (2020) sample in the same redshift range probed by KURVS observations have $M_\star \sim 10^{11.5}\,\mathrm{M}_\odot$ (see Figs 8 and 9), and hence probe the high-mass end of the main sequence at $z \sim 1.5$. The high-mass end of the main sequence is where 'typical discs' become rarer, because this regime samples beyond the characteristic $M_\star$ of the stellar mass function, and where galaxies are expected to grow massive bulges and subsequently quench (Dekel & Birnboim 2006; Zolotov et al. 2015). Therefore, such massive galaxies might not be representative of the bulk of the star-forming population and the tension between observations and simulations might be related to quenching mechanisms and/or a poor understanding of bulge growth mechanisms and spheroid formation. Indeed, Genzel et al. (2020) noted that the preference for a cored dark matter profile is strongly correlated with the central bulge mass.

The idea that differences between observed and simulated dark matter fractions are associated with the baryonic properties of galaxies, rather than being a problem of the underlying dark matter backbone, is supported by the fact that these arise when considering the dependence of $f_{\mathrm{DM}}(R_{\mathrm{eff}})$ on the stellar mass surface density (right-hand panel of Fig. 8). Indeed, cosmological models such as EAGLE struggle to reproduce the sizes and light profiles of massive galaxies at $z \sim 0$ (Rodriguez-Gomez et al. 2019; de Graaff et al. 2022), and Illustris-TNG recovers the low dark matter fractions of massive star-forming discs at high-redshift, but for too-small effective radii (Übler et al. 2021). It is plausible that the discrepancies are driven by the sub-grid modelling of physical processes of galaxy formation and feedback, and its complex interplay with the underlying dark matter halo distribution. In fact, state-of-the-art simulations such as EAGLE and Illustris-TNG seem to overpredict the dark matter content of massive spirals in the local Universe, possibly as a result of the feedback implementation (the 'failed feedback problem'; Posti, Fraternali & Marasco 2019; Marasco et al. 2020). Future work will thus also be required from the simulation perspective to understand what drives the difference between the dark matter halo and baryonic properties of simulated and observed galaxies in the distant Universe.

ACKNOWLEDGEMENTS

The authors would like to thank the referee for their constructive report on our paper. The authors acknowledge the Virgo Consortium for making their simulation data available. The EAGLE simulations were performed using the DiRAC-2 facility at Durham, managed by the ICC, and the PRACE facility Curie based in France at TGCC, CEA, Bruyères-le-Châtel. SG acknowledges the support of the Cosmic Dawn Center of Excellence funded by the Danish National Research Foundation under the grant 140. LC acknowledges support from the Australian Research Council Discovery Project and Future Fellowship funding schemes (DP210100337, FT180100066). CH acknowledges funding from a United Kingdom Research and Innovation grant (code: MR/V022830/1). EI acknowledges funding by ANID FONDECYT Regular 1221846. DO is a recipient of an Australian Research Council Future Fellowship (FT190100083) funded by the Australian Government. KAO acknowledges support by the European Research Council (ERC) through Advanced Investigator grant to CS Frenk, DMIDAS (GA 786910). AP and MS thank Ian Smail for useful discussions and valuable inputs on the analysis. AP also thanks Nicolas Bouché for useful discussions regarding the GALPAK^{3D} code. This work was supported by STFC through grants ST/T000244/1 and ST/P000541/1. This work has made use of NASA's Astrophysics Data System.

DATA AVAILABILITY

The data used in this paper are available through the ESO archive.

Downloaded from https://academic.oup.com/mnras/article/524/2/2814/7221661 by University of Durham user on 31 October 2023

REFERENCES

Barnabè M. et al., 2012, MNRAS, 423, 1073
Bell E. F., de Jong R. S., 2001, ApJ, 550, 212
Bland-Hawthorn J., Gerhard O., 2016, ARA&A, 54, 529
Bosma A., 1978, PhD thesis, University of Groningen, the Netherlands
Bouché N., Carfantan H., Schroetter I., Michel-Dansac L., Contini T., 2015, AJ, 150, 92
Bouché N. F. et al., 2022, A&A, 658, A76
Bovy J., Rix H.-W., 2013, ApJ, 779, 115
Bryant J. J. et al., 2015, MNRAS, 447, 2857
Burkert A. et al., 2010, ApJ, 725, 2324
Casertano S., 1983, MNRAS, 203, 735
Catinella B., Giovanelli R., Haynes M. P., 2006, ApJ, 640, 751
Chabrier G., 2003, PASP, 115, 763
Conselice C. J., 2014, ARA&A, 52, 291
Courteau S., Dutton A. A., 2015, ApJ, 801, L20
Crain R. A. et al., 2015, MNRAS, 450, 1937
Cresci G. et al., 2009, ApJ, 697, 115
da Cunha E., Charlot S., Elbaz D., 2008, MNRAS, 388, 1595
da Cunha E. et al., 2015, ApJ, 806, 110
Davé R., Thompson R., Hopkins P. F., 2016, MNRAS, 462, 3265
Davé R., Anglés-Alcázar D., Narayanan D., Li Q., Rafieferantsoa M. H., Appleby S., 2019, MNRAS, 486, 2827
Davidzon I. et al., 2017, A&A, 605, A70
de Blok W. J. G., McGaugh S. S., Rubin V. C., 2001, AJ, 122, 2396
de Graaff A., Trayford J., Franx M., Schaller M., Schaye J., van der Wel A., 2022, MNRAS, 511, 2544
Dekel A., Birnboim Y., 2006, MNRAS, 368, 2
Di Teodoro E. M., Fraternali F., Miller S. H., 2016, A&A, 594, A77
Dubois Y., Peirani S., Pichon C., Devriendt J., Gavazzi R., Welker C., Volonteri M., 2016, MNRAS, 463, 3948
Dubois Y. et al., 2021, A&A, 651, A109
Dutton A. A. et al., 2013, MNRAS, 428, 3183
Efstathiou G., Lake G., Negroponte J., 1982, MNRAS, 199, 1069
Elbaz D. et al., 2018, A&A, 616, A110
Epinat B., Amram P., Balkowski C., Marcelin M., 2010, MNRAS, 401, 2113
Epinat B. et al., 2012, A&A, 539, A92
ESO CPL Development Team, 2015, EsoRex: ESO Recipe Execution Tool. Astrophysics Source Code Libraryhttp://www.eso.org/sci/software/cpl/download.html record ascl:1504.003
Ferrero I. et al., 2017, MNRAS, 464, 4736
Förster Schreiber N. M., Wuyts S., 2020, ARA&A, 58, 661
Förster Schreiber N. M. et al., 2009, ApJ, 706, 1364
Förster Schreiber N. M. et al., 2018, ApJS, 238, 21
Franco M. et al., 2020, A&A, 643, A30
Fraternali F., Karim A., Magnelli B., Gómez-Guijarro C., Jiménez-Andrade E. F., Posses A. C., 2021, A&A, 647, A194
Freeman K. C., 1970, ApJ, 160, 811
Frenk C. S., White S. D. M., Efstathiou G., Davis M., 1985, Nature, 317, 595
Furlong M. et al., 2017, MNRAS, 465, 722
Genel S. et al., 2014, MNRAS, 445, 175
Genzel R. et al., 2006, Nature, 442, 786
Genzel R. et al., 2017, Nature, 543, 397
Genzel R. et al., 2020, ApJ, 902, 98
Gillman S. et al., 2019, MNRAS, 486, 175
Gillman S. et al., 2020, MNRAS, 492, 1492
Gillman S. et al., 2022, MNRAS, 512, 3480
Girard M. et al., 2021, ApJ, 909, 12
Gogate A. R., Verheijen M. A. W., van der Hulst J. M., Jaffé Y. L., 2022, MNRAS, 519, 4279
Grogin N. A. et al., 2011, ApJS, 197, 35
Guo Y. et al., 2013, ApJS, 207, 24
Harrison C. M. et al., 2017, MNRAS, 467, 1965
Herrera-Camus R. et al., 2022, A&A, 665, L8
Jiménez E., Lagos C. d. P., Ludlow A. D., Wisnioski E., 2022, MNRAS, preprint (arXiv:2210.09673)
Johnson H. L. et al., 2018, MNRAS, 474, 5076
Kaasinen M. et al., 2020, ApJ, 899, 37
Kassin S. A. et al., 2007, ApJ, 660, L35
Kassin S. A. et al., 2012, ApJ, 758, 106
Krumholz M. R., Burkhart B., Forbes J. C., Crocker R. M., 2018, MNRAS, 477, 2716
Lang P. et al., 2017, ApJ, 840, 92
Lelli F., McGaugh S. S., Schombert J. M., 2016, AJ, 152, 157
Lelli F., De Breuck C., Falkendal T., Fraternali F., Man A. W. S., Nesvadba N. P. H., Lehnert M. D., 2018, MNRAS, 479, 5440
Lelli F. et al., 2023, A&A, 672, A106
Lovell M. R. et al., 2018, MNRAS, 481, 1950
Luo B. et al., 2017, ApJS, 228, 2
Madau P., Dickinson M., 2014, ARA&A, 52, 415
Marasco A., Posti L., Oman K., Famaey B., Cresci G., Fraternali F., 2020, A&A, 640, A70
Martinsson T. P. K., Verheijen M. A. W., Westfall K. B., Bershady M. A., Schechtman-Rook A., Andersen D. R., Swaters R. A., 2013a, A&A, 557, A130
Martinsson T. P. K., Verheijen M. A. W., Westfall K. B., Bershady M. A., Andersen D. R., Swaters R. A., 2013b, A&A, 557, A131
McAlpine S. et al., 2016, Astron. Comput., 15, 72
McGaugh S. S., Schombert J. M., Bothun G. D., de Blok W. J. G., 2000, ApJ, 533, L99
Miller S. H., Ellis R. S., Sullivan M., Bundy K., Newman A. B., Treu T., 2012, ApJ, 753, 74
Mobasher B. et al., 2015, ApJ, 808, 101
Molina J., Ibar E., Smail I., Swinbank A. M., Villard E., Escala A., Sobral D., Hughes T. M., 2019, MNRAS, 487, 4856
Muzzin A. et al., 2013, ApJS, 206, 8
Übler H. et al., 2017, ApJ, 842, 121
Übler H. et al., 2018, ApJ, 854, L24
Übler H. et al., 2019, ApJ, 880, 48
Übler H. et al., 2021, MNRAS, 500, 4597
Ostriker J. P., Peebles P. J. E., 1973, ApJ, 186, 467
Ostriker J. P., Peebles P. J. E., Yahil A., 1974, ApJ, 193, L1
Pillepich A. et al., 2019, MNRAS, 490, 3196
Posti L., Fraternali F., Marasco A., 2019, A&A, 626, A56
Price S. H. et al., 2021, ApJ, 922, 143
Puglisi A. et al., 2019, ApJ, 877, L23
Puglisi A. et al., 2021, MNRAS, 508, 5217
Rizzo F., Vegetti S., Powell D., Fraternali F., McKean J. P., Stacey H. R., White S. D. M., 2020, Nature, 584, 201
Rizzo F., Vegetti S., Fraternali F., Stacey H. R., Powell D., 2021, MNRAS, 507, 3952
Rizzo F., Kohandel M., Pallottini A., Zanella A., Ferrara A., Vallini L., Toft S., 2022, A&A, 667, A5
Rodriguez-Gomez V. et al., 2019, MNRAS, 483, 4140
Rubin V. C., Ford W. K. J., Thonnard N., 1978, ApJ, 225, L107
Sargent M. T., Béthermin M., Daddi E., Elbaz D., 2012, ApJ, 747, L31
Schaller M. et al., 2015, MNRAS, 451, 1247
Schaye J. et al., 2015, MNRAS, 446, 521
Schreiber C. et al., 2015, A&A, 575, A74
Sharma G., Salucci P., Harrison C. M., van de Ven G., Lapi A., 2021, MNRAS, 503, 1753
Sharma G., Salucci P., van de Ven G., 2022, A&A, 659, A40
Sharples R. et al., 2013, The Messenger, 151, 21
Simons R. C. et al., 2016, ApJ, 830, 14
Simons R. C. et al., 2017, ApJ, 843, 46
Simons R. C. et al., 2019, ApJ, 874, 59
Soto K. T., Lilly S. J., Bacon R., Richard J., Conseil S., 2016, MNRAS, 458, 3210
Springel V. et al., 2018, MNRAS, 475, 676
Stott J. P. et al., 2016, MNRAS, 457, 1888
Suess K. A. et al., 2022, ApJ, 937, L33
Sweet S. M. et al., 2019, MNRAS, 485, 5700
Swinbank A. M. et al., 2017, MNRAS, 467, 3140
Tacchella S. et al., 2018, ApJ, 859, 56
Tacconi L. J., Genzel R., Sternberg A., 2020, ARA&A, 58, 157

Downloaded from https://academic.oup.com/mnras/article/524/2/2814/7221661 by University of Durham user on 31 October 2023

Tadaki K.-i. et al., 2017, ApJ, 841, L25
Tiley A. L. et al., 2019a, MNRAS, 482, 2166
Tiley A. L. et al., 2019b, MNRAS, 485, 934
Tiley A. L. et al., 2021, MNRAS, 506, 323
Trachternach C., de Blok W. J. G., Walter F., Brinks E., Kennicutt R. C. J., 2008, AJ, 136, 2720
Tully R. B., Fisher J. R., 1977, A&A, 54, 661
Turner O. J., Harrison C. M., Cirasuolo M., McLure R. J., Dunlop J., Swinbank A. M., Tiley A. L., 2017a, preprint (arXiv:1711.03604)
Turner O. J. et al., 2017b, MNRAS, 471, 1280
van der Wel A. et al., 2012, ApJS, 203, 24
van der Wel A. et al., 2014, ApJ, 788, 28
Vogelsberger M. et al., 2014a, MNRAS, 444, 1518
Vogelsberger M. et al., 2014b, Nature, 509, 177
Vogelsberger M., Marinacci F., Torrey P., Puchwein E., 2020, Nat. Rev. Phys., 2, 42
Weiner B. J. et al., 2006, ApJ, 653, 1027
Wellons S., Faucher-Giguère C.-A., Anglés-Alcázar D., Hayward C. C., Feldmann R., Hopkins P. F., Kereš D., 2020, MNRAS, 497, 4051
Wisnioski E. et al., 2015, ApJ, 799, 209
Wisnioski E. et al., 2019, ApJ, 886, 124
Wuyts S. et al., 2016, ApJ, 831, 149
Zolotov A. et al., 2015, MNRAS, 450, 2327

APPENDIX A: THE KURVS-CDFS DATASET

We include in this section the kinematic maps (Figs A1–A3) and position-velocity diagrams (Fig. A4) for all galaxies in the KURVS-CDFS pointing analysed in this work. We provide measurements of the maximal rotation curve extent and velocity at the last observed data point on the rotation curve, as well as measurements of the rotation velocity at R'_{3D} and R'_{6D} in Table A1.

Notes on individual sources

(i) KURVS-1 or cdfs_24904. This is a compact, nearly spheroidal galaxy, as suggested by the *HST* high-resolution imaging and measurements of the near-infrared half-light radius. KURVS ultra-deep observations show a somewhat regular velocity field in the inner regions of the galaxy as well as some asymmetries at large radii possibly suggesting the presence of a secondary component. The galaxy shows high velocity dispersion and dispersion-dominated dynamics.

(ii) KURVS-2 or cdfs_26404. The *HST* imaging indicates that this is a large clumpy spiral galaxy nearly face-on. Clumps are also observed in the Hα flux map. KMOS observations indicate a regular velocity field with some asymmetries at both edges of the rotation curve. However, the outer regions of the rotation curve are associated with large uncertainties, and it is difficult to establish if these asymmetries are tracing perturbations at large radii. The galaxy is overall regularly rotating, but we exclude it from the 'discs sample' because of its $v_{\rm rot}/\sigma_0$ ratio.

(iii) KURVS-3 or cdfs_26954. This is a massive spiral galaxy with a prominent bulge in the *HST* imaging. The galaxy has a

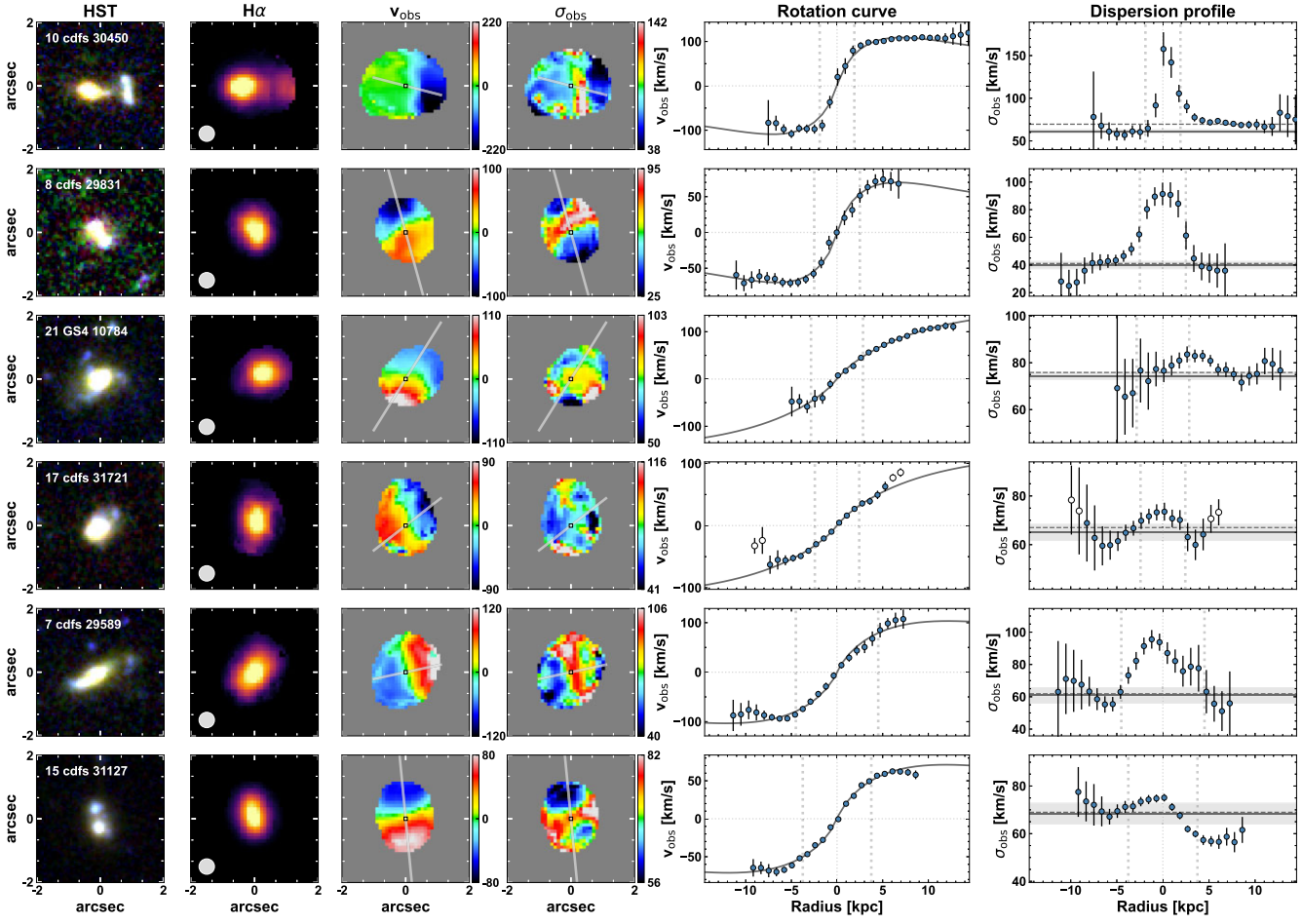

Figure A1. Same as Fig. 3.

Downloaded from https://academic.oup.com/mnras/article/524/2/2814/7221661 by University of Durham user on 31 October 2023

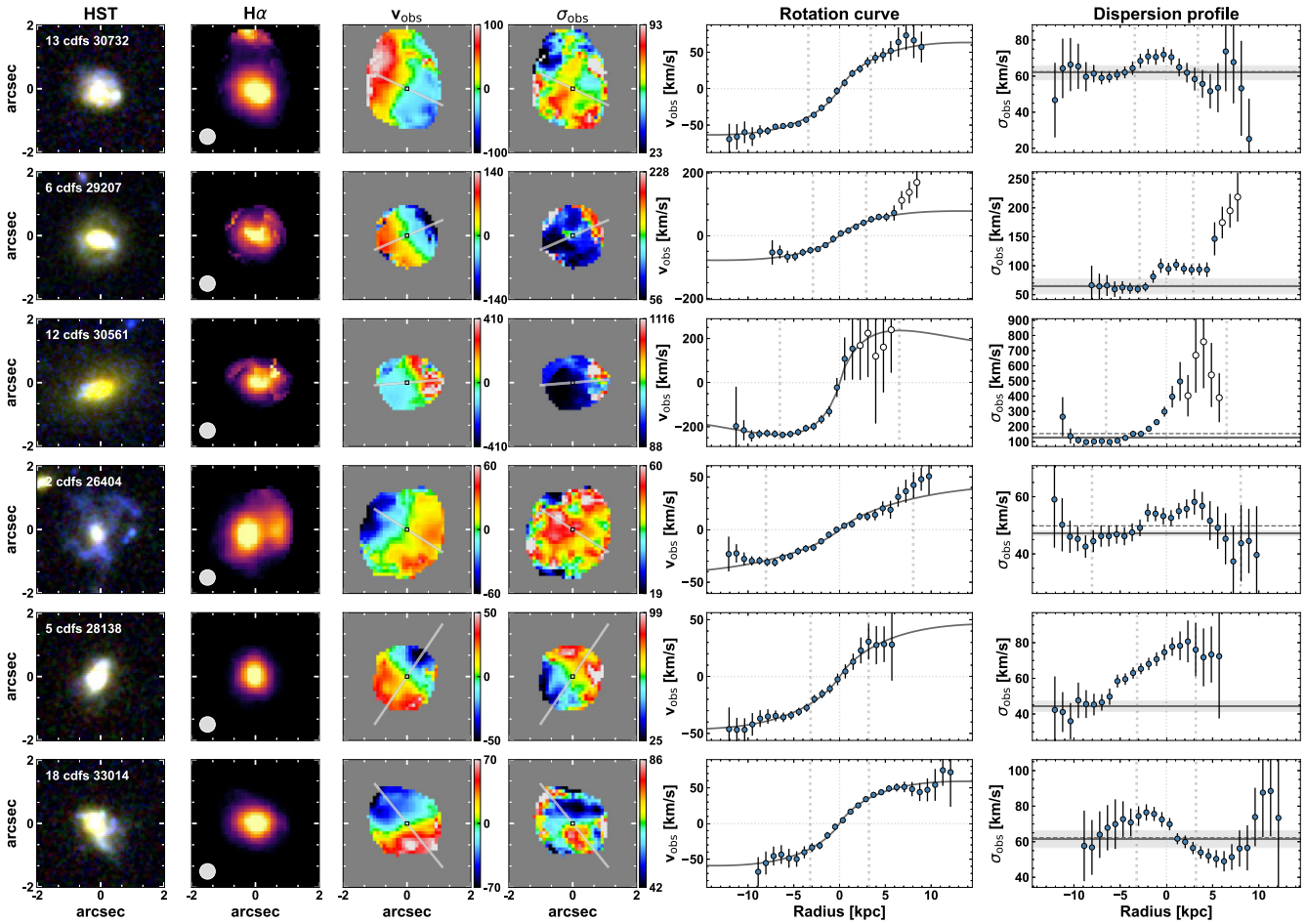

Figure A2. *continuation*.

regular velocity field and centrally peaked velocity dispersion profile, suggesting rotationally supported dynamics. This is also reflected in the v_{rot}/σ_0 ratio, which is well above unity for this galaxy. The galaxy shows a declining rotation curve at $\sim 3\sigma$ significance.

(iv) KURVS-4 or cdfs_27318. This spiral galaxy shows a bright bulge in the *HST* imaging. The *HST* image also shows indication of a possible companion at large radius, beyond the extent of the cut-out shown in Fig. A3. The velocity map and velocity dispersion are highly perturbed, and the small velocity gradient indicate that the galaxy is nearly face on. The highly perturbed nature of this galaxy is also indicated by $v_{rot}/\sigma_0 \sim 0.2$. The rotation curve of this galaxy is significantly declining at large radii. However, measurements of t are highly uncertain in this galaxy as a result of its very perturbed kinematics.

(v) KURVS-5 or cdfs_28138. This is a clumpy galaxy with a regular but asymmetric velocity field. The galaxy also shows an asymmetric velocity dispersion profile. We exclude it from the 'discs sample' because of its v_{rot}/σ_0 ratio.

(vi) KURVS-6 or cdfs_29207. The *HST* morphology suggests a low-inclination spiral galaxy with a bright central component and spiral arms. The velocity map indicates regular rotation, and the velocity dispersion map is centrally peaked. There are a few 'noisy' pixels at the edge of both the rotation curve and the velocity dispersion profile. From a visual inspection of the KMOS cube, these pixels seem to be associated with a broad component having high velocity dispersion. Excluding these pixels from the fit to the rotation curve does not change the outer rotation curve shape. The galaxy is not included in the 'discs sample' because of its v_{rot}/σ_0 ratio.

(vii) KURVS-7 or cdfs_29589. This is a highly inclined spiral galaxy. The velocity field suggests regular rotation, although the rotation curve is somewhat asymmetric. The velocity dispersion profile is centrally peaked. This suggests that the galaxy is rotationally supported in its dynamics, as also indicated by the v_{rot}/σ_0 ratio.

(viii) KURVS-8 or cdfs_29831. The *HST* images indicate a small clumpy galaxy. KURVS observations and measurements of the v_{rot}/σ_0 ratio indicate rotationally supported dynamics, as suggested by a regular velocity field and centrally peaked velocity dispersion profile. The galaxy shows a declining outer rotation curve at $\sim 3\sigma$ significance.

(ix) KURVS-9 or cdfs_30267. This is a clumpy spiral galaxy with a bright central component in the *HST* imaging. The regular velocity field and centrally peaked velocity dispersion suggest rotation-dominated dynamics.

(x) KURVS-10 or cdfs_30450. This galaxy is formally classified as a rotationally supported disc as it displays a regularly rotating velocity field, a continuous velocity gradient along the kinematic major axis, has $v_{rot}/\sigma_0 \geq 1.5$ and the position of the steepest velocity gradient coincides with the peak of the velocity dispersion. However, the *HST* imaging indicates the presence of two merging companions. This suggests that the kinematics signatures observed in KURVS data

Downloaded from https://academic.oup.com/mnras/article/524/2/2814/7221661 by University of Durham user on 31 October 2023

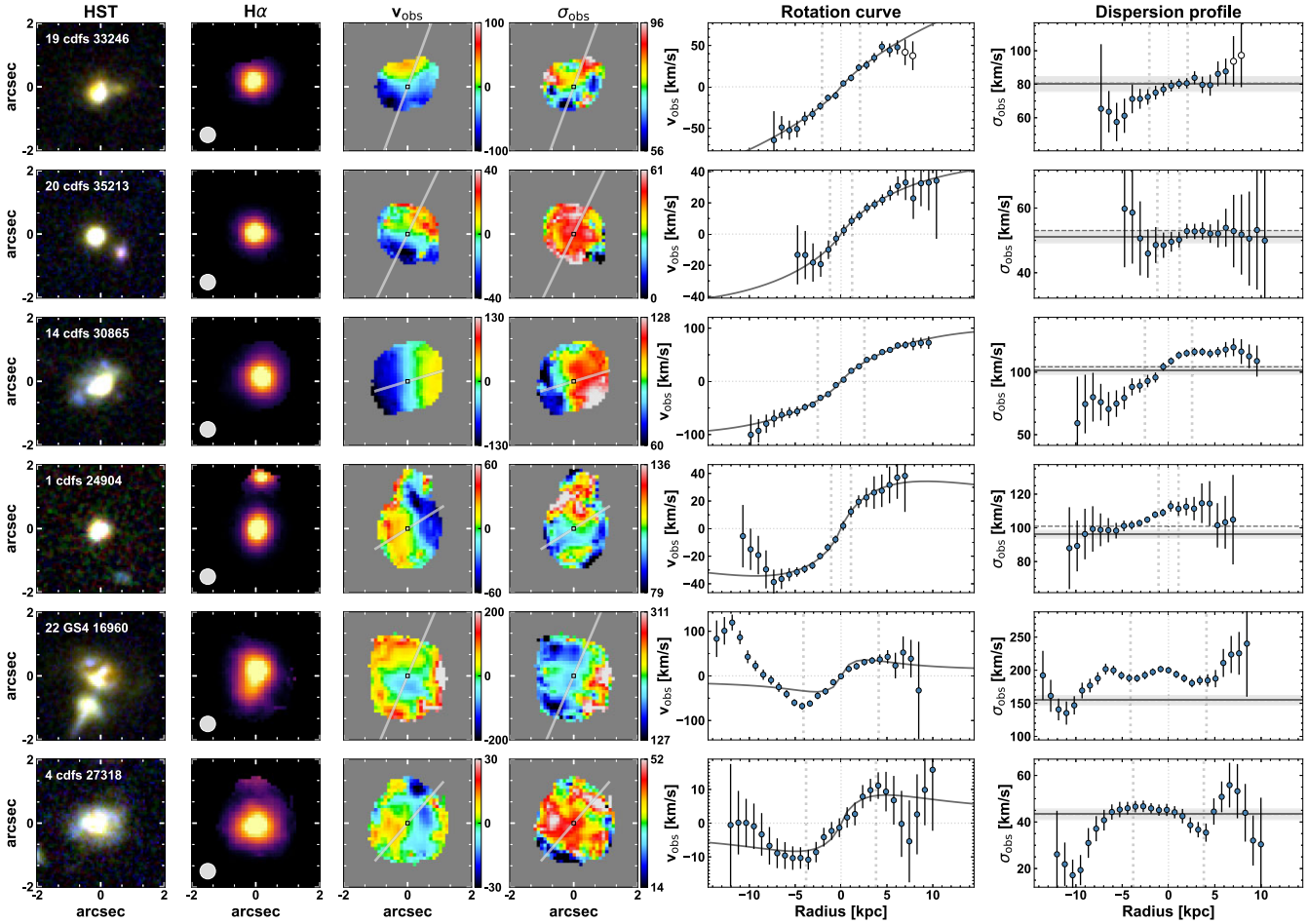

Figure A3. *continuation.*

are associated with the orbital motion of a merging pair, rather than with a rotating disc. This is expected, given that that there is a high probability of misclassifying merging pairs as discs in seeing-limited observations (Simons et al. 2019; Rizzo et al. 2022). The highly asymmetric rotation curve as well as the high velocity dispersion measured in the inner regions of the velocity dispersion map support the merging pair interpretation. Because of the complexity associated with modelling a merging pair, we exclude this galaxy from analysis of the dark matter fractions.

(xi) KURVS-11 or cdfs_30557. This is a large clumpy edge-on spiral with regular kinematics and centrally peaked velocity dispersion profile.

(xii) KURVS-12 or cdfs_30561. This is a red compact galaxy in the *HST* images. The rotation curve and velocity dispersion profile are highly asymmetric. A visual inspection of the KMOS cube suggests that the outer regions of the kinematic maps are associated with a broad component. Excluding these pixels from the fit to the rotation curve does not change the outer rotation curve shape. The galaxy is not included in the 'discs sample' because of its clearly perturbed kinematics, which also implies a v_{rot}/σ_0 ratio below our 'discs sample' cut. The rotation curve of this galaxy is significantly declining at large radii. However, measurements of t are highly uncertain in this galaxy as a result of its very perturbed kinematics.

(xiii) KURVS-13 or cdfs_30732. This galaxy is a clumpy spiral according to the *HST* images. The source displays a regular velocity field and somewhat asymmetric rotation curve. The velocity dispersion profile is peaked at the centre, and noisy and irregular towards the outer regions. However, the outer velocity dispersion profile is consistent with being flat within the uncertainties. The velocity and velocity dispersion maps suggest a rotating disc, and the galaxy is included in the 'discs sample' given its v_{rot}/σ_0 ratio.

(xiv) KURVS-14 or cdfs_30865. This is a clumpy galaxy with a regular velocity field and rotation curve. The galaxy also shows an asymmetric velocity dispersion profile, and a high velocity dispersion. As a result, the galaxy is not included in the 'discs sample'.

(xv) KURVS-15 or cdfs_31127. A clumpy galaxy with a regular velocity field and symmetric rotation curve. The velocity dispersion profile is peaked at the centre, although it shows some asymmetries in the outer regions. The kinematic maps suggest a rotation-dominated disc, consistent with the v_{rot}/σ_0 ratio.

(xvi) KURVS-16 or cdfs_31671. The *HST* imaging indicates a clumpy edge-on disc. The galaxy shows a regular velocity field and rotation curve, and a centrally peaked velocity dispersion profile. This suggests that the galaxy is rotationally supported in its dynamics, as also indicated by the high v_{rot}/σ_0 ratio. From a visual inspection of the KMOS cube, there are a few 'noisy' pixels at the edge of the rotation curve and the velocity dispersion profile. Excluding these

Downloaded from https://academic.oup.com/mnras/article/524/2/2814/7221661 by University of Durham user on 31 October 2023

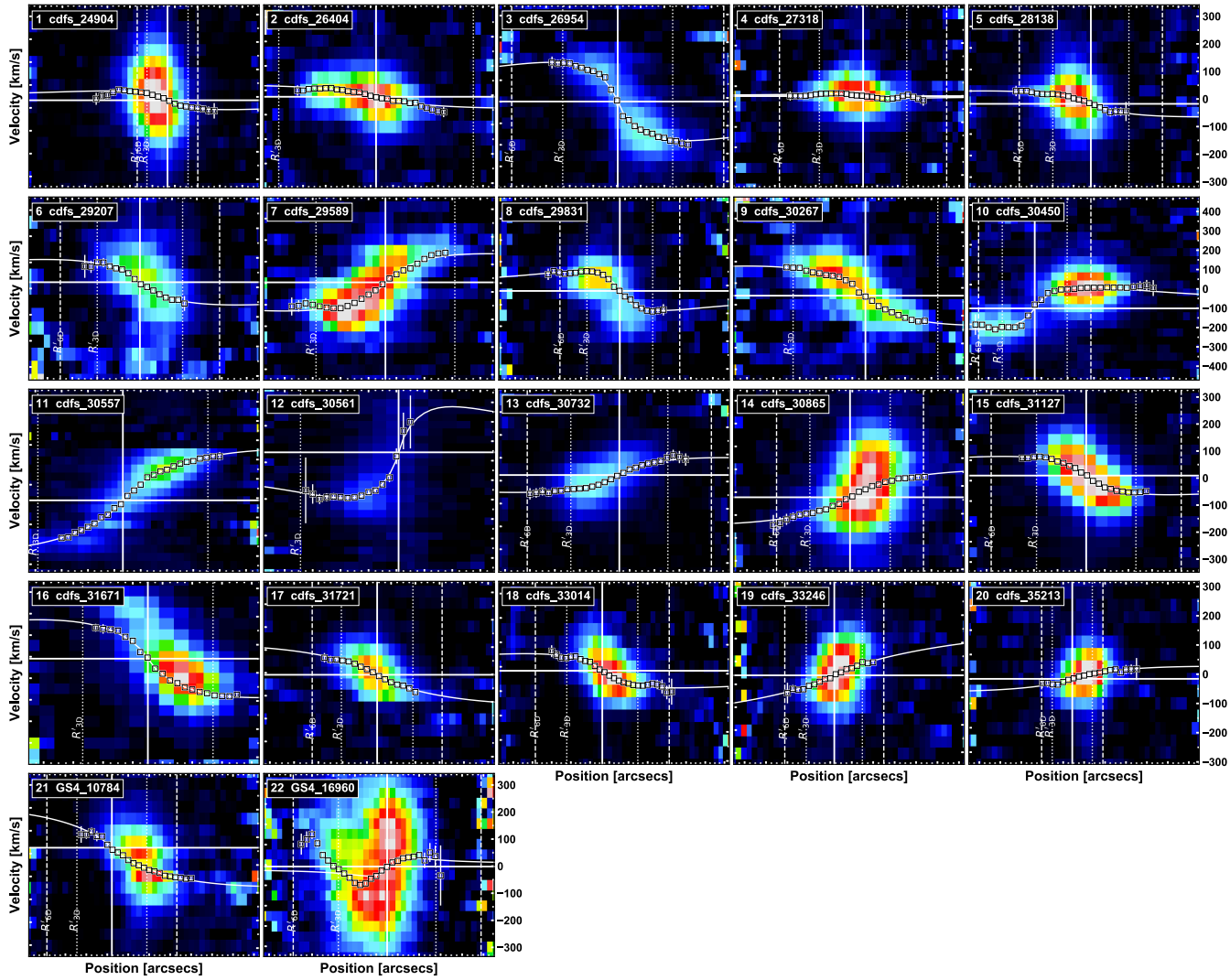

Figure A4. Position–velocity diagrams for the KURVS galaxies. The colour scale represents the flux intensity, with black and white indicating the lowest and highest flux levels, respectively. The colour scale is weighted by the inverse of the sky spectrum to the fifth power. Open black squares indicate the observed rotation velocity at each pixel extracted from the velocity map and used to obtain the best-fitting exponential disc model (white solid curve). Solid vertical and horizontal lines indicate the radial and velocity position of the rotation curve centre, respectively. White, dotted (dashed) vertical lines are displayed at ±3 times (±6 times) the disc scale radius R_d. A visual inspection of this plot suggests that the best-fitting exponential disc model provide a good extrapolation of the position–velocity diagrams at large radii.

pixels from the fit to the rotation curve does not change the outer rotation curve shape.

(xvii) KURVS-17 or cdfs_31721. The *HST* imaging indicates a clumpy galaxy. The object shows a regular velocity field and rotation curve, with a few 'noisy' pixels at the edge. Clipping these pixels does not significantly affect measurements of the the outer rotation curve shape. The velocity dispersion profile shows a central peak and some asymmetries towards the outer regions. However, the outer pixels have large uncertainties.

(xviii) KURVS-18 or cdfs_33014. The *HST* morphology suggests an irregular galaxy. The velocity map indicates overall rotation. However, the outer rotation curve displays symmetric disturbances. The object presents a perturbed velocity dispersion map and an asymmetric velocity dispersion profile. The perturbations in the outer kinematics might indicate interactions with a companion. The galaxy is excluded from the 'disc sample' because of the relatively low v_{rot}/σ_0 ratio.

(xix) KURVS-19 or cdfs_33246. The *HST* image shows a small clumpy galaxy. KMOS observations indicate an asymmetric velocity field and velocity dispersion profile. The galaxy has a high velocity dispersion. Excluding 'noisy' pixels at the edge of the rotation curve and the velocity dispersion profile does not significantly change the outer rotation curve shape. The galaxy is excluded from the 'disc sample' because of its low v_{rot}/σ_0 ratio.

(xx) KURVS-20 or cdfs_35213. This is a compact galaxy, as suggested by the small half-light radius. The *HST* image indicates two round-shaped components with low inclinations, it is unclear if these are interacting or are tracing clumpy emission. The object shows a highly asymmetric rotation curve and an irregular velocity dispersion profile, nearly flat. The kinematic properties of the source might also indicate merging activity. The irregular nature of this galaxy is also reflected in the low v_{rot}/σ_0 ratio.

(xxi) KURVS-21 or GS4_10784. The *HST* image indicates a bulgy galaxy with blue emission at the edges. It is unclear if this

Downloaded from https://academic.oup.com/mnras/article/524/2/2814/7221661 by University of Durham user on 31 October 2023

Table A1. Rotational velocities of KURVS-CDFS galaxies at different radii.

KURVS ID	$R_{H\,\alpha,\,max}$ kpc	$v_{H\,\alpha,\,max}$ km s^{-1}	$v_{R'_{3D}}$ km s^{-1}	$C_{BS,R'_{3D}}$ –	$v_{R'_{6D}}$ km s^{-1}
(1)	(2)	(3)	(4)	(5)	(6)
1	10.7	49.3 ± 7.9	40.9 ± 1.8	1.138	42.9 ± 2.1
2	12.1	48.4 ± 13.5	52.4 ± 7.6	1.009	59.4 ± 14.1
3	11.7	209.8 ± 12.4	217.1 ± 3.7	1.040	198.7 ± 5.0
4	12.0	8.0 ± 2.3	10.4 ± 1.0	1.047	7.4 ± 1.1
5	12.1	55.6 ± 12.4	46.3 ± 4.8	1.060	55.1 ± 6.7
6	8.1	82.1 ± 30.1	77.2 ± 6.8	1.065	87.0 ± 7.3
7	11.4	105.4 ± 8.5	104.8 ± 5.0	1.036	102.5 ± 7.4
8	11.0	68.8 ± 7.2	79.4 ± 16.7	1.078	72.5 ± 15.5
9	10.2	136.9 ± 9.4	137.7 ± 6.8	1.030	143.1 ± 11.5
10	15.2	93.4 ± 15.1	115.9 ± 4.4	1.099	114.4 ± 4.0
11	12.4	246.6 ± 6.2	240.0 ± 7.7	1.021	276.1 ± 7.1
12	11.2	258.2 ± 71.2	256.6 ± 78.6	1.017	171.7 ± 53.3
13	12.1	94.3 ± 10.5	85.2 ± 3.4	1.054	94.6 ± 5.4
14	9.8	105.6 ± 12.6	80.8 ± 7.6	1.076	103.6 ± 9.9
15	9.2	112.2 ± 3.6	111.0 ± 2.8	1.048	113.9 ± 3.3
16	10.9	139.4 ± 6.8	136.0 ± 3.0	1.045	138.7 ± 1.2
17	9.9	120.9 ± 9.5	86.5 ± 6.6	1.080	115.0 ± 8.6
18	12.1	76.1 ± 8.7	68.1 ± 2.7	1.059	75.9 ± 4.5
19	7.9	95.4 ± 15.5	67.2 ± 17.9	1.092	94.6 ± 25.3
20	10.4	80.2 ± 24.6	44.9 ± 11.7	1.131	53.0 ± 13.8
21	12.7	145.6 ± 15.9	100.4 ± 6.4	1.068	133.4 ± 8.7
22	13.6	28.9 ± 2.6	42.1 ± 2.9	1.042	27.5 ± 1.8

Note. (1) KURVS ID; (2) Maximal extent of the observed rotation curve; (3) Inclination-corrected velocity at the maximal extent of the observed rotation curve; (4) Inclination- and beam-smearing corrected velocity at R'_{3D}; (5) Multiplicative factor applied to the observed velocity at R'_{3D} to correct for beam smearing (see Section 3.3 for details); (6) Inclination-corrected velocity at R'_{6D}. Note that, this quantity is not corrected for beam smearing which we expect to be negligible at these large radii, as discussed in Section 3.3.

emission traces spiral arms or disturbances. The rotation curve and velocity dispersion profile are asymmetric. There are issues with measurements of the radial and velocity offset obtained from fitting the one-dimensional rotation curve. The object is formally rotation-dominated given the high v_{rot}/σ_0 ratio, and we include it in our 'discs sample'. However, its kinematic properties suggest perturbations. Indeed, it is difficult to model the velocity field with GALPAK^{3D}, and this is independent from measurements of the dynamical centre.

(xxii) KURVS-22 or GS4_16960. The *HST* morphology is highly perturbed, as well as the velocity and velocity dispersion maps. As discussed in the main text, the galaxy is detected in X-rays and in the far-infrared, possibly indicating that an AGN and/or a merger-driven starburst are powering its H α emission.

APPENDIX B: CIRCULAR VELOCITY AND OUTER ROTATION CURVE SLOPES OF $z \sim 0$ DISCS

We extract one-dimensional rotation curves for THINGS galaxies by applying a similar procedure to that used on the KURVS sample. We obtain individual velocity maps from the THINGS webpage.[3] We extract rotation curves along the kinematic position angle indicated in table 1 of Trachternach et al. (2008) and within a 2 pixel radius pseudo-slit. We measure the relevant kinematic parameters (i.e. the slope of the rotation curve t and the velocity at R_{6D}) from the observed rotation curve smoothed with a uniform filter with a 100 km s^{-1} window. This is to mitigate the effect of local disturbances in the rotation curve. We checked, however, that measurements of the t parameter for this sample are not affected by the size of the smoothing window. We exclude from the plot the four THINGS galaxies with an observed rotation curve that does not extend to R_{6D}. For the Catinella et al. (2006) sample, we measured rotation curve slopes from the best-fitting one-dimensional models to their rotation curve templates in bins of I-band magnitude.

We do not apply any pressure-support corrections to measure circular velocities in galaxies in the local Universe. This is because the velocity dispersion is much lower in $z \sim 0$ galaxies than in the high-redshift Universe (e.g. Übler et al. 2019), hence the pressure support would correspond to a small correction to the rotation velocity.

[3] https://www2.mpia-hd.mpg.de/THINGS/Data.html

[1] *School of Physics and Astronomy, University of Southampton, Highfield SO17 1BJ, UK*
[2] *Centre for Extragalactic Astronomy, Department of Physics, Durham University, South Road, Durham DH1 3LE, UK*
[3] *Max-Planck-Institut für Astronomie, Königstuhl 17, D-69117 Heidelberg, Germany*
[4] *Cosmic Dawn Center (DAWN), Copenhagen, Denmark*
[5] *DTU-Space, Technical University of Denmark, Elektrovej 327, DK-2800 Kgs. Lyngby, Denmark*
[6] *International Centre for Radio Astronomy Research, University of Western Australia, 35 Stirling Highway, Crawley, WA 6009, Australia*
[7] *Institute for Computational Cosmology, Durham University, South Road, Durham DH1 3LE, United Kingdom*
[8] *Institute for Data Science, Department of Physics, Durham University, South Road, Durham DH1 3LE, United Kingdom*
[9] *European Southern Observatory, Karl-Schwarzschild-Str 2, D-86748 Garching b. München, Germany*

Downloaded from https://academic.oup.com/mnras/article/524/2/2814/7221661 by University of Durham user on 31 October 2023

[10]*ARC Centre of Excellence for All Sky Astrophysics in 3 Dimensions (ASTRO 3D), Australia*
[11]*Centre for Astrophysics and Supercomputing, Swinburne University of Technology, PO Box 218, Hawthorn, VIC 3122, Australia*
[12]*School of Mathematics, Statistics and Physics, Newcastle University, Newcastle upon Tyne NE1 7RU, UK*
[13]*Instiuto de Física y Astronomía, Universidad de Valparaíso, Avda. Gran Bretaña 1111, Valparaíso, Chile*
[14]*Department of Space, Earth and Environment, Chalmers University of Technology, Onsala Space Observatory, 439 92 Onsala, Sweden*
[15]*Australian Research Council Centre of Excellence for All-Sky Astrophysics, 44 Rosehill Street Redfern, NSW 2016, Australia*
[16]*Department of Physics, Durham University, South Road, Durham DH1 3LE, United Kingdom*
[17]*Lorentz Institute for Theoretical Physics, Leiden University, PO Box 9506, NL-2300 RA Leiden, the Netherlands*
[18]*Leiden Observatory, Leiden University, PO Box 9513, NL-2300 RA Leiden, the Netherlands*
[19]*Centre for Advanced Instrumentation, Department of Physics, Durham University, South Road, Durham DH1 3LE, UK*

This paper has been typeset from a TEX/LATEX file prepared by the author.

Downloaded from https://academic.oup.com/mnras/article/524/2/2814/7221661 by University of Durham user on 31 October 2023

© The Author(s) 2023.
Published by Oxford University Press on behalf of Royal Astronomical Society. This is an Open Access article distributed under the terms of the Creative Commons Attribution License (https://creativecommons.org/licenses/by/4.0/), which permits unrestricted reuse, distribution, and reproduction in any medium, provided the original work is properly cited.